https://doi.org/10.5194/essd-2024-492
Preprint. Discussion started: 26 June 2025

Open Access Earth System Science Data Discussions

Long-term meteorological and carbon, water and energy flux data from the Boreal Ecosystem Research and Monitoring Sites, Saskatchewan, Canada

Alan Barr[1,2], T. Andrew Black[3], Warren Helgason[4,1,2], Andrew Ireson[5,1], Bruce Johnson[1], J. Harry McCaughey[6,†], Zoran Nesic[3], Charmaine Hrynkiw[7], Amber Ross[7], Newell Hedstrom[7]

[1] Global Institute for Water Security, University of Saskatchewan, Saskatoon, S7N 3H5, Canada
[2]Centre for Hydrology, University of Saskatchewan, Saskatoon, S7N 5C8, Canada
[3] Faculty of Land and Food Systems, University of British Columbia, Vancouver, V6T 1Z4, Canada
[4] Civil, Geological, and Environmental Engineering, University of Saskatchewan, Saskatoon, S7N 5A9, Canada
[5]School of Environment and Sustainability, University of Saskatchewan, Saskatoon, S7N 5C8, Canada
[6] Department of Geography and Planning, Queen's University, Kingston, K7L 3N6, Canada
[7] Environment and Climate Change Canada, Saskatoon, S7N3H5, Canada
[†]deceased

Correspondence: Warren Helgason (warren.helgason@usask.ca)

Abstract. The Boreal Ecosystem Research and Monitoring Sites (BERMS) are a network of flux tower research sites located near the southern boundary of the Boreal Plains Ecozone in Saskatchewan, Canada. This network includes four principal sites that characterize the region's dominant vegetation types: mature trembling aspen (Old Aspen, OA, 1997-2017), mature black spruce (Old Black Spruce, OBS, 1997-present), mature jack pine (Old Jack Pine, OJP, 1997-present), and a minerotrophic patterned fen (Fen, 2002-present). The dataset reported here include continuous long-term records of site meteorological variables (air temperature, humidity, barometric pressure, precipitation, wind speed and direction), vertical profiles of soil temperature and volumetric water content, surface energy balance components (soil and biomass heat fluxes, photosynthetic heat flux, and eddy covariance-derived latent and sensible heat fluxes), and carbon fluxes (net ecosystem production, gross primary productivity, and ecosystem respiration). The strengths of the data set are its length and completeness, spanning up to 27 years; the care given to the measurement of net radiation and the minor surface energy balance terms; the care given to the measurement of precipitation and other hydrologic variables; and the proximity of the sites, which enables inter-site comparisons of the responses of the carbon and water balances to climatic controls. The data are available at https://doi.org/10.20383/103.01318 (Helgason et al., 2024).

1 Introduction

The Boreal Ecosystem Research and Monitoring Sites (BERMS) are a network of flux-tower research sites located near the southern edge of the Boreal Plains Ecozone in Saskatchewan, Canada. The BERMS sites were established in 1993 as part of the Southern Study Area of the Boreal Ecosystem-Atmosphere Study (BOREAS) (Sellers et al., 1997). The primary BOREAS objectives were to better understand of the role of the boreal forest in the global carbon cycle and climate system; to create integrated data sets that could be used to evaluate and improve climate, hydrologic,

https://doi.org/10.5194/essd-2024-492
Preprint. Discussion started: 26 June 2025

and ecosystem C-cycle models; and to better anticipate the potential effects of climate change on this important biome. The BOREAS data from 1994-1996 are available at the Oak Ridge National Laboratory Distributed Active Archive Center (ORNL DAAC). The BERMS program has benefitted greatly from BOREAS' multidisciplinary design, its integration of measurements with modelling, and the priority given to data management. When BOREAS ended in 1996, the Southern Old Aspen (OA), Old Black Spruce (OBS), and Old Jack Pine (OJP) flux towers continued as BERMS, and the Southern Fen flux tower was restarted in 2002. BERMS played a leading role in the Fluxnet-Canada Research Network (FCRN, 2002-2007) and the Canadian Carbon Program (2007-2011), and has contributed to the Changing Cold Regions Network (2012-2017), Global Water Futures (2017-2023), the Global Water Futures Observatories (starting 2023), the North American Carbon Program, AmeriFlux, and FLUXNET.

The BERMS program was originally operated and funded by Environment and Climate Change Canada, Natural Resources Canada, and Parks Canada, in partnership with researchers at the University of British Columbia (UBC), Queen's University, and the University of Saskatchewan. Since 2012, the Global Institute for Water Security (GIWS), University of Saskatchewan, has led the program, with strong continuing involvement of UBC at OA and OBS through 2017. After 2017, the OA site was decommissioned, and GIWS assumed full responsibility for operations at OBS, OJP, and Fen.

The Boreal Plains Ecozone covers 701,750 km^2 (7% of Canada's land area). It extends from northeastern British Columbia, across portions of Alberta and central Saskatchewan, to Lake Winnipeg in Manitoba. The ecozone is characterized by a northern continental climate, with long, cold winters and short cool summers. Over 60% of the Boreal Plains is forested including coniferous evergreen needleleaf (42%), broadleaf deciduous (37%), and mixed forests (20%), with the topography typically characterized by a flat to gently rolling, hummocky and kettled terrain (ESTR Secretariat, 2014). The Boreal Plains is a diverse land-cover mosaic with a spatial pattern of climax vegetation controlled by soil drainage and available soil moisture (Ireson et al., 2015). In general, jack pine forests are located on the well-drained sandy uplands, mixed-wood and aspen forests on the well-drained loamy uplands, black spruce forests and treed wetlands in the lowland depressions, and peatlands in the poorly-drained deeper depressions. The four long-term BERMS sites represent the dominant vegetation types in the Boreal Plains Ecozone, including mature forest stands of trembling aspen (Old Aspen OA), black spruce (Old Black Spruce OBS), and jack pine (Old Jack Pine OJP), and a minerotrophic patterned fen (Fen).

The BERMS sites are strategically located near the southern edge of the western boreal forest, a region that is expected to be highly sensitive to climate change (Ireson et al., 2015). The geographic transition from grasslands and croplands (to the south) to boreal forest (to the north) coincides with a shift in the water balance, with diminishing water deficits to the north (Hogg, 1997). If future climate warming in this region is associated with more frequent and severe water deficits, as is likely to be the case, the southern edge of the boreal forest is expected to shift northward, with biome shifts occurring primarily after wildfire (Ireson et al., 2015).

The BERMS data sets have been widely used, in better understanding the ecophysiological processes that control the exchanges of carbon, water and energy between the ecosystem and the atmosphere (e.g., Liu et al., 2019; Liu et al., 2022), in synthesis studies (e.g. Ireson et al., 2015; Helbig et al., 2020), for model evaluation and improvement (e.g. Keenan et al., 2012; Richardson et al., 2012), and as ground-truth in the development of remote sensing methods (e.g.

https://doi.org/10.5194/essd-2024-492
Preprint. Discussion started: 26 June 2025

Lambert et al., 2013; Pulliainen et al., 2017). The strengths of the data include: its length and completeness, spanning over 25 years; the consistency in instrumentation and data processing; the care given to the measurement of net radiation and the minor energy balance terms; the care given to the measurement of precipitation and other hydrologic variables, including streamflow from the White Gull Creek watershed containing the OBS and OJP sites; and the close proximity of the sites to each other, which enables intercomparison of the responses of different vegetation types to climatic forcings.

This paper documents the core flux and meteorological data sets at the four long-term BERMS sites. The objectives are to provide background information about the sites; to document the data sets including instrumentation and data-logging history, data post-processing, quality assurance, and gap-filling methods; to assess data quality; to identify a few known problems; and describe if and how the problems have been resolved. The data are archived through the Federal Research Data Repository of the Digital Research Alliance of Canada and are available at https://doi.org/10.20383/103.01318 (Helgason et al., 2024). Additional measurements not reported here include water table depth, snow depth, and periodic surveys of snow water equivalent and tree biometry.

2 Study Area

The BERMS study area is in the Boreal Plains Ecozone, near the southern edge of the boreal forest (Fig. 1). The continental climate is characterized by having a long and dry cold season and a short growing season. The most recent climate normals for nearby climate stations are for Waskesiu Lake (53.92 °N, -106.07 °W, 1971-2000), with mean annual, January and July air temperatures of 0.4, -17.9 and 16.2 °C, respectively, and mean annual precipitation of 467 mm, 30% of which fell as snow; and Prince Albert Airport (53.22 °N, -105.67 °W, 1991-2020), with mean annual, January and July air temperatures of 1.4, -17.2 and 17.9 °C, respectively, and mean annual precipitation of 432 mm (1991-2020), 27% of which fell as snow (based on the 1981-2010 normals).

The eastern portion of the BERMS study area includes the White Gull Creek watershed (603 km^2), which has been gauged for continuous streamflow measurement since 1993 (Water Survey of Canada, 2024), annual streamflow, 1994-2022, corresponding to a mean (± s.d.) runoff depth of 125 ± 64 mm y^{-1}.

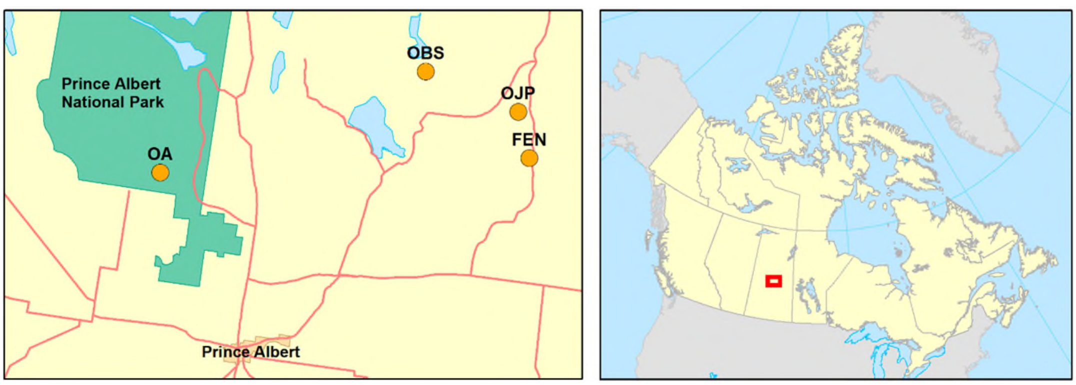

https://doi.org/10.5194/essd-2024-492
Preprint. Discussion started: 26 June 2025

Earth System Science Data Discussions
Open Access

Figure 1. Location of the Old Aspen (OA), Old Black Spruce (OBS), Old Jack Pine (OJP), and Fen sites in the province of Saskatchewan, Canada.

2.1 Flux-tower sites

The long-term BERMS flux-tower sites include two mature evergreen needleleaf forests (black spruce and jack pine), one deciduous broadleaf forest (trembling aspen) and one wetland fen. Site properties are given in Tables 1 (location and vegetation) and 2 (soils).

2.1.1 Old Aspen

The Old Aspen (OA) site is located in Prince Albert National Park, about 70 km NW of Prince Albert. The forest stand has two distinct layers: an overstory of trembling aspen (*Populus tremuloides* Michx. 95 %) with scattered balsam poplar (*Populus balsamifera* L. 5 %) and a 2-m understory of dense beaked hazelnut (*Corylus cornuta* Marsh.) (Griffis et al., 2003, 2004). The stand was established by natural regeneration after a forest fire in 1919 (Kljun et al., 2006), with subsequent fires eliminating the conifer seed source and resulting in a nearly pure deciduous stand (Dave Weir, Prince Albert National Park, *personal communication*). The soil is an Orthic Gray Luvisol (Blanken et al., 1997) having a 10-cm LFH organic horizon overtop a 30-cm silt loam mineral soil horizon overlying clay-rich glacial till subsurface materials. The water table depths range from 1 to 5 m below the ground surface, varying spatially according to location in the hummocky terrain, with ponded water in low-lying depressions during wet years. Further description of this site can be found in Blanken et al. (1997).

2.1.2 Old Black Spruce

Old Black Spruce (OBS) is located 115 km northeast of Prince Albert, Saskatchewan. The forest stand was established by natural regeneration after a forest fire in 1879 (Kljun et al., 2006, Krishnan et al., 2008). The site is dominated by black spruce (*Picea mariana* [Mill.] BSP), but also contains ~10% tamarack (*Larix laricina* Du Roi). The understory consists of sparse shrubs (e.g., *Rhododendron groenlandicum* (Oeder), Kron & Judd and *Vaccinium vitisidaea* L.). The predominant groundcover is feather moss (*Hylocomium splendens* [Hedw.] Schimp., *Pleurozium schreberi* (Brid.) Mitt., with patches of hummocky peat (*Sphagnum* spp.) in wet areas and reindeer lichen (*Cladonia* spp.) in drier areas. The soil is Peaty Orthic Gleysol with a 20-30 cm deep peat layer overlying waterlogged sand, with imperfect to poor drainage. The surface is relatively flat with a hummock-hollow micro topography in wetter areas with occasional surface water in the hollows (Jarvis et al., 1997). Depth to water table varies between 0 and 1 m below the ground surface. Further description can be found in Jarvis et al. (1997), Gower et al. (1997), and Gaumont-Guay et al. (2014).

2.1.3 Old Jack Pine

Old Jack Pine (OJP) is located on a glacial outwash plain about 140 km northeast of Prince Albert. The dominant tree species is jack pine (*Pinus banksiana* Lamb.). The dominant understory ground cover is reindeer lichen (*Cladonia mitis* [Sandst.] Hustich) with isolated groups of green alder (*Alnus crispa* [Ait.] Pursh) and feathermoss (*Pleurozium*

https://doi.org/10.5194/essd-2024-492
Preprint. Discussion started: 26 June 2025

spp.) (Gower et al., 1997). The stand was established by natural regeneration after a forest fire in 1914 (Zha at al., 2009). The soil is a degraded Eutric Brunisol/Orthic Eutric Brunisol and the site topography is relatively flat with few gently rolling ridges (Baldocchi et al., 1997). The sandy soil is nutrient poor and well drained with the water table lying at least 5 m below the ground surface. For additional site details, see Baldocchi et al. (1997) and Gower et al. (1997).

2.1.4 Fen

The Fen site is a moderately rich, minerotrophic patterned fen surrounded by black spruce and jack pine forests, 120 km northeast of Prince Albert, Saskatchewan. The fen is orientated northwest-southeast and contains 8.5 km^2 of peatland (Sonnentag et al., 2010). The peat depth varies from 1 m near the edges up to 2-3 m in the center of the fen. Sedges (*Carex* spp. And *Eriophorum* spp.) and buckbean (*Menyanthes trifoliate* L.) are the dominant herbaceous plants. The dominant woody species include bog birch (*Betula pumila* L.) and tamarack (*Larix laricina* [Du Roi] K. Koch). As of 2019, the bog birch and tamarack species have significantly diminished due to persistent high water levels in the fen. Except for during dry years the water table is generally at or above the peat surface. Further description of this site is available in Suyker et al. (1997) and Sonnentag et al. (2010).

https://doi.org/10.5194/essd-2024-492
Preprint. Discussion started: 26 June 2025

Table 1. Characteristics of the BERMS sites

	OA	OBS	OJP	Fen
Location	53.629°N, 106.198°W	53.987°N, 105.118°W	53.916°N, 104.692°W	53.802°N, 104.618°W
Elevation (m)*	596	591	510	485
Dominant tree species	Trembling aspen	Black spruce	Jack pine	Scattered bog birch and tamarack
Dominant understory species	Beaked hazelnut	Feathermoss	Reindeer lichen	Buckbean and sedges
Stand height (m)	21	11	14	n/a
Stand density (stems ha^{-1})	964 (1994) 726 (2004) 542 (2010) 474 (2016)	5900 (1994)	1317 (1994) 1119 (2004) 1061 (2008) 916 (2016) 645 (2023)	n/a
Leaf area index**	2.4 aspen 2.0 hazelnut	3.8	2.6	
Soil drainage	Moderate	Poor	Good	

* The site elevations have been updated based on a recent reassessment and differ from the earlier estimates. In particular, the earlier value of 579 m at OJP was found to be in error.

** Barr et al. (2004); Chen et al. (2006)

Table 2 Soil properties at the BERMS flux towers, by horizon*.

	Soil Horizon	Depth (m)	Bulk Density (kg m^{-3})	Organic C Content (%)	Soil Texture Class (% Sand, Silt, Clay)
OA	L	-0.10 to -0.07	140	42.9	Organic
	F	-0.07 to -0.04	220	38.8	Organic
	H	-0.04 to 0.00	386	33.1	Organic
	Ae, Aeg	0.00 to 0.21	1316	0.66	Loam (49,41,10)
	Bt, Btg, Bmk	0.21 to 0.69	1502	0.32	Sandy Clay Loam (49,27,24)
	Ck	0.69 to 0.83	1438	0.31	Sandy Clay Loam (54,24,22)
OBS	Peat**	-0.20 to -0.10	44	42.6	Organic
	Peat**	-0.10 to 0.00	120	44.9	Organic
	Ae	0.00 to 0.02	1250	1.40	Sandy loam (76,20,4)
	AB	0.02 to 0.05	1520	0.98	Sandy loam (73,21,6)
	Bt	0.05 to 0.17	1660	0.36	Sandy loam (64,29,7)
	Bfj	0.17 to 0.42	1660	0.10	Sand (96,2,2)
	Ck	0.42 to 0.72	1660	0.05	Sand (96,2,2)
OJP	LFH	-0.02 to 0.00	243	25.1	Organic
	Ae	0.00 to 0.02	1225	1.00	Sand (94,3,3)
	AB	0.02 to 0.06	1447	0.64	Sand (93,4,3)
	Bm	0.06 to 0.34	1483	0.13	Sand (94,3,3)
	C1	0.34 to 0.83	1517	0.02	Sand (96,2,2)

* excerpted from Anderson et al. (2000).

** At OBS, the depth of the peat layer within the flux-tower footprint is highly variable, in some places approaching 1.0 m; these estimates are from the locations of the soil temperature and water content profiles and may be shallower than the mean depth.

3 Instrumentation and Measurements

A list of the core instrumentation is included in Table A1.

3.1 Air temperature, humidity, pressure, and wind

Air temperature T_a (°C) and relative humidity RH (%) were measured at three or four heights at each site using temperature/humidity probes (models HMP35CF, HMP45C, and HMP155A, Vaisala Inc., Oy, Finland) mounted 30 cm away from southeast corner of the flux tower in 12-plate (or 14-plate for HMP155A) unventilated Gill radiation shields (models 41002 and 41005, Campbell Scientific, Logan, UT, USA). At the forested sites, the measurement heights included above-canopy (approximately twice the canopy height – 37 m at OA, 25 m at OBS, and 28 m at OJP)

https://doi.org/10.5194/essd-2024-492
Preprint. Discussion started: 26 June 2025

and within-canopy locations (1, 4, and 18 m at OA, 1 and 6 m at OBS, and 1 and 10 m at OJP). At the uppermost level, air temperature was also measured using unshielded fine-wire type-E chromel-constantan thermocouples (25 or 75 µm), and a shielded and ventilated thermocouple and platinum resistance thermometer (mode RTD-810, Omega Engineering, Norwalk, CT, USA) in an aspirated radiation shield (model 076B, Met One Instruments, Grants Path, OR, USA). The measurements in the aspirated radiation shield had frequent dropouts and periods when the fan failed and so were used only in filling gaps when the other measurements failed.

The RH data were corrected to ensure that the maximum value did not exceed 100%. The measured RH maximum varied among sensors; in particular, some of the earlier model HMP35CF sensors routinely reached a maximum RH as high as 110%. A simple correction was applied based on a sensor-specific estimate of the upper RH envelope (RH_x), estimated as the 99th percentile of the warm-season measurements (based on air temperatures of between 0 and 20 ºC, the range over which RH reached 100%). The corrected value RH* was computed as:

$$\mathrm{RH}^* = (\mathrm{RH}/\mathrm{RH_x})*100\%, \quad (1)$$

Wind speed and direction were measured at the top of the flux tower using a propeller anemometer (model 05103, R.M. Young, Traverse City, MI, USA). Atmospheric pressure p_a (kPa) was measured in the instrumentation hut at ~2 m above ground level using a barometric pressure sensor (model SBP270, Setra Systems Inc., Boxborough, MA, USA at OA, OBS, and OJP, and model PTA427A, Vaisala Inc., Oy, Finland at Fen).

Vapor pressure e_a (kPa) was computed from RH and the saturation vapor pressure over water e_{sa} (kPa), which in turn was computed as a function of T_a using the six-parameter formulation of Hyland and Wexler (1983), given as Eq. 2.5 in Flatau, Walko and Cotton (1992). Specific humidity q_a (kg kg^{-1}) was then calculated from e_a and p_a as:

$$q = 0.622 e_a/(p_a - 0.378 e_a), \quad (2)$$

3.2 Precipitation

Precipitation was measured at OA, OBS, OJP and Fen using an accumulating gauge (Belfort model 3000 (Belfort Instruments, Baltimore, MD, USA) for all years at OA, 1997 to 2011 at OBS, 1997 to 2010 at OJP, and 1997 to 2010 at Fen; and Geonor model T-200B (GEONOR Inc., Augusta, NJ, USA) at OBS starting Jan 2012, OJP starting Sept 2010, and Fen starting Jan 2011. The resolution of the Belfort 300 gauge was 1 mm, whereas the resolution of the Geonor T-200B was less than 0.01 mm, as determined by the data-logger resolution.

At the three forest sites, the gauges were situated in the centre of small forest clearings, at approximately one tree height from the clearing edges, to minimize wind effects on snowfall catch efficiency. At OA, the gauge was mounted on a raised platform at ~ 3 m above ground level (agl), ~50 m northeast of the flux tower. At OBS, the Belfort gauge (and the replacement Geonor gauge) were mounted on the roof of the instrument hut until May 2023, at ~5 m agl. In May 2023, the Geonor gauge was moved off the hut and mounted on a pedestal at ~2 m agl. At OJP, the Belfort gauge was mounted on a raised platform at ~3 m agl, ~150 m southeast of the flux tower. The replacement Geonor gauge was mounted on a pedestal at ~2 m agl, ~125 m east of the flux tower. At Fen, up to 2011, the Belfort gauge was mounted on a pedestal in the open fen at ~2 m agl, where it was exposed to the wind. The replacement Geonor gauge was installed in Sept 2010 in a sheltered forest clearing atop the instrument hut at ~5 m agl. In May 2023, it was moved to a nearby location in the forest clearing and mounted on pedestal at ~ 2 m agl. In all cases, the precipitation

https://doi.org/10.5194/essd-2024-492
Preprint. Discussion started: 26 June 2025

gauges were equipped with a single Alter shield to reduce wind effects on snowfall catch efficiency. A tipping bucket rain gauge (Texas Instruments model TE525 then Hydrological Services TB3) was also deployed near each accumulating gauge, and was used to fill gaps and to determine rainfall event timing for the Belfort gauge which had only 1 mm resolution. A propeller anemometer (model 05103, R.M. Young Co, Traverse City, MI, USA) or 3-cup anemometer (model 12102, Gill Instruments Ltd., Lymington, UK) was installed nearby to measure windspeed at gauge height.

The accumulating gauges were serviced twice a year. Each spring, the bucket was charged with 1.5-2 L of water and 500 mL of 0W-20 motor oil. Each fall, the bucket was charged with 4 L of antifreeze and 500 mL of 0W-20 motor oil. Motor oil was added year-round to minimize evaporative losses. Antifreeze was added to prevent freezing of the bucket contents in the winter months.

The cumulative precipitation time series was smoothed using a neutral aggregating filter (Ross et al., 2020) to eliminate noise and extract the 30-min interval precipitation amounts, aggregated to a minimum value of 0.1 mm. The algorithm removes random noise and accounts for diurnal oscillations in the bucket weight signal but does not account for drift, which means that it will not perform well if the accumulating gauge has periods of water loss by evaporation (Smith et al., 2018). Precipitation was then partitioned into rainfall and snowfall based on air temperature and humidity (Harder and Pomeroy, 2013). At the three forest sites and at Fen after 2010, the gauges were sheltered from the wind and no adjustments were needed to correct for wind-induced undercatch of snowfall. At the Fen from 2003 to 2010, when the Belfort gauge was situated in the open and exposed to wind, measured snowfall was corrected for wind-induced undercatch based on the catch efficiency CE, estimated from the measured windspeed U (m s^{-1}) and air temperature T_a (°C) at gauge height using the empirical transfer functions developed by the WMO Solid Precipitation Intercomparison Experiment (SPICE) (Smith et al., 2020, equation 1):

$$\mathrm{CE} = \begin{cases} e^{-aU\left(1-\tan^{-1}(bT_a)+c\right)}; & T_a \leq T_a^* \\ 1; & T_a > T_a^* \end{cases}, \tag{3}$$

where: a = 0.0348; b = 1.366; c = 0.779; and T_a^* was set to 2 °C. The CE adjustment at the Fen increased annual snowfall by an average of 34% and annual P by an average of 7%, 2003-2010.

Snow depth (continuous) and snow water equivalent (periodic snow surveys) were also measured but are not included in this data set.

3.3 Soil temperature and water content

Soil temperature T_s was measured using copper-constantan (type T) thermocouples at two locations, with vertical profiles of six depths (2, 5, 10, 20, 50, 100 cm) below the ground surface (relative to the top of the upper organic soil horizon, Table 2). Vertical soil volumetric water content VWC profiles were measured at two or more locations per site, but each site had its own configuration of sensors and depths. OA used time-domain-reflectometer TDR probes at depths of 0-15, 15-30, 30-60, 60-90, and 90-120 cm. Up to 2007, the measurements were made using four profiles of Moisture Point MP-917 type-B probes (Environmental Services Inc., Victoria, B.C., Canada) located in a low-lying area of the site. That location partially flooded in 2004 and remained flooded through 2007, and so in late summer 2007 three profiles of CSI TDR100 probes (Campbell Scientific, Logan, UT, USA) were installed at a new location

https://doi.org/10.5194/essd-2024-492
Preprint. Discussion started: 26 June 2025

with slightly higher elevation, more typical of the flux footprint, followed by the decommissioning of the original system in 2008. In addition, shallow soil VWC at OA was measured using soil water content reflectometers (model CS615, Campbell Scientific, Logan, UT, USA), with two locations at depths of 2.5 and 7.5 cm. OBS, OJP and Fen each had two vertical profiles of soil water content reflectometers (model CS615 at OBS and OJP, model CS616 at Fen), at depths of 7.5 and 22.5 cm at OBS; 0-15, 15-30, 30-60, 60-90, 90-120, and 120-150 cm at OJP; and 0-15 and 15-30 cm at Fen. The CS615 and CS616 probe orientation was either horizontal, diagonal, or vertical to measure a single depth or a 15- or 30-cm layer, respectively. At all sites but Fen, the measured VWC was adjusted to correct for sensitivity to soil temperature as per the manufacturer's instructions. The temperature-correction relationship for the CS615 probes, which was developed for a 10 to 30 °C temperature range, was applied to all measurements of 5 °C and above, and when the temperature was below 5 °C, the correction for 5 °C was applied.

3.4 Radiation

Upwelling and downwelling shortwave radiation flux densities were measured above the canopy using paired pyranometers (model CM11 or CMP11, Kipp and Zonen, Delft, The Netherlands) at the three mature forest sites and a four-component net radiometer (models CNR1 or CNR4, Kipp and Zonen, Delft, The Netherlands) at Fen. Upwelling and downwelling longwave radiation were measured above the canopy using paired pyrgeometers (model PIR, Eppley Laboratory, Newport, RI, USA) at the three mature forest sites (replaced by model CG4, Kipp and Zonen, Delft, The Netherlands at OJP in Sept 2013), and a four-component net radiometer (model CNR1 or CNR4, Kipp and Zonen, Delft, The Netherlands) at Fen. A redundant CNR1 or CNR4 was added to the forest sites in July 2003 (OA), Apr 2007 (OBS), and Sept 2010 (OJP). The upward-facing radiometers were mounted atop the scaffold flux tower in ventilated housings to minimize dew and frost on the sensor domes. The net radiometers and the downward-facing radiometers were mounted on a horizontal boom that extended 4 m to the south of the flux towers, 5 to 10 m above the forest canopies and 15 m above Fen. The net radiometers were heated in winter to prevent frost formation on the sensor domes. Above-canopy net radiation was calculated from the shortwave and longwave components, giving priority to the paired CM11/CMP11 pyranometers and PIR/CG4 pyrgeometers when available.

The theoretical top-of-atmosphere incoming shortwave radiation was computed for each site based on the formulations in Iqbal (1983, chapter 1), integrated analytically to calculate a 30-min mean.

Upwelling and downwelling photosynthetically-active radiation PPFD were measured above at all sites using PPFD (quantum) sensors (model LI-190, LI-COR, Lincoln, NB, USA, replaced twice during the measurement period but not since 2007 (see Section 5.1.1 below)). Downwelling PPFD was also measured below the canopy at the forest sites.

3.5 Data logging and telemetry

Most meteorological data were logged every 5 sec and output as 30-min means, using an array of data loggers (models CR7, CR10x, CR21x, CR23x, and CR1000, Campbell Scientific, Logan, UT, USA). The exceptions were soil VWC, which was sampled once every 4 hours up to 2012 at OJP and up to 2021 at OBS and every 30 min thereafter; and accumulated precipitation, which was sampled once every 30 min. The data were uploaded once daily from the on-

https://doi.org/10.5194/essd-2024-492
Preprint. Discussion started: 26 June 2025

site dataloggers to the BERMS database at the Global Institute for Water Security in Saskatoon. Since 2012, the data have been managed using the WISKI Water Information System (Kisters, Roseville, CA, USA).

3.6 Quality assurance and gap filling

All meteorological data were screened daily using automated limit checking followed monthly by manual, graphical inspection and identification and exclusion of questionable values. The exclusion criteria were conservative, so that only extreme outliers were flagged and excluded.

Gaps in meteorological data were filled annually based on relationships with related time series (similar measurements from the same site or a nearby site). The gap-filling method varied by gap size and variable type, based on an evaluation of several approaches as described and evaluated in Appendix B. For most variables, gaps of 2 hours or less were filled using simple linear interpolation, gaps of 2 to 12 hours based on the interpolated difference between the variable and a related time series, gaps of 12 hours to 3 months using moving-window regression often limited to the same time of day, and gaps of 3 months to 1 year using moving-window regression based on the five previous years of data, fitted by time of year and sometimes also time of day. Further details are given in Appendix B.

Missing precipitation data from the accumulating gauges were filled in two ways. When the measured precipitation accumulation increased over the data gap so that the total was known, the missing data were filled using the best related time series, either from the on-site tipping bucket or the accumulating gauge at the nearest site, but scaled to match the known total. When the missing precipitation total was unknown, the values from the best related time series were used directly.

3.7 Fluxes

3.7.1 Surface energy, water, and carbon balances

The surface energy balance:

$$R_n = H + \lambda E + Q, \tag{4}$$

was measured by eddy covariance (EC sensible H and latent λE heat flux densities), with independent measurements of the net radiation flux density R_n and the minor surface-energy-balance terms Q, where Q is the sum of three terms: the soil heat flux density Q_g, the rate of change of heat storage in the above-ground biomass Q_b (forest sites only), and the energy flux density associated with the CO_2 flux (through photosynthesis and respiration) Q_p. Our sign convention is that radiation fluxes are positive when towards the surface whereas H and λE are positive when away from the surface. All terms in (1) have units of (W m^{-2}). Eq. (4) pertains to the warm-season only; it does not include terms for freeze-thaw events or heat storage in the snowpack, neither of which were measured in this study.

The vertical water balance:

$$P = E + \Delta S + O, \tag{5}$$

was quantified using measurements of the rates of precipitation P, evapotranspiration E, and the rate of change of water storage in the soil and snowpack ΔS, with the rate of lateral outflow O from overland runoff, interflow, and groundwater baseflow calculated as a residual. Typical units for the variables in (2) are (mm d^{-1}) or (mm y^{-1}). Note

https://doi.org/10.5194/essd-2024-492
Preprint. Discussion started: 26 June 2025

that complementary streamflow measurements from the White Gull basin (Barr et al., 2012), which includes the OJP and OBS flux towers, are available from Water Survey of Canada (2023).

The surface carbon balance may be written as

$$\mathrm{NEP} = \mathrm{GEP} - R_e, \tag{6}$$

where the net ecosystem production NEP results as the balance between C uptake through gross ecosystem photosynthesis GEP and C release through ecosystem respiration R_e. Our sign convention is that NEP is positive when the ecosystem is gaining C, and that both GEP and R_e are given positive signs (Barr et al., 2007).

In situations where the atmospheric flux is the only significant mechanism for C gain or loss by the ecosystem, such as the forest sites in this study (but not the Fen, where a significant net import or export of dissolved organic C may occur in the lateral water flow), NEP can be estimated directly from eddy-covariance measurements of net ecosystem exchange NEE, as:

$$\mathrm{NEP} = -\mathrm{NEE}, \tag{7}$$

When reporting C fluxes, we often use NEE in units (μmol C m^{-2} s^{-1}) to report the measured 30-min fluxes, and NEP, GEP and R_e to report the ecosystem C balance at various time scales, e.g. in units (g C m^{-2} d^{-1}) or (g C m^{-2} y^{-1}). The difference in sign convention between NEP and NEE reflects an ecosystem versus atmospheric perspective; NEP is positive when the ecosystem is a C sink, gaining C from the atmosphere, whereas NEE is positive when the atmosphere is gaining C and the ecosystem is a C source.

3.7.2 Eddy-covariance fluxes

The EC method measures the friction velocity u_* and the surface fluxes of sensible heat H, latent heat λE, and carbon dioxide (net ecosystem exchange NEE). The latter three are calculated as the sum of two terms: the turbulent eddy flux, measured above the vegetation canopy using the EC instrumentation; and the flux divergence (air-column storage change) between the ground surface and the EC measurement level, calculated based on profile measurements of the scalar in question. H and λE (Eq. 4) are computed as the sum of the EC fluxes at height z (H_z and λE_z) and the EC storage fluxes (S_H and $S_{\lambda E}$):

$$H = H_z + S_H, \tag{8a}$$

where:

$$S_H = \int_0^z \rho c_p \frac{dT_a}{dt} dz, \tag{8b}$$

and

$$\lambda\mathrm{E} = \lambda\mathrm{E}_z + S_{\lambda E}, \tag{9a}$$

where:

$$S_{\lambda E} = \int_0^z \rho\lambda \frac{dq}{dt} dz, \tag{9b}$$

T_a is the air temperature (ºC), q is the specific humidity (kg kg^{-1}), ρ is the density of moist air (kg m^{-3}), c_p is the specific heat of moist air (J kg^{-1} $^{o}C^{-1}$), and λ is the latent heat of vaporization (J kg^{-1}). The three storage terms (Eqs. 8b, 9b, and 10b) are computed from the simple linear differences of 30-min mean T_a, q, and c, using the half hour before and the half hour after the 30-min period for which the storage change is being calculated.

https://doi.org/10.5194/essd-2024-492
Preprint. Discussion started: 26 June 2025

Evapotranspiration E (mm d^{-1} or mm y^{-1}) is calculated from λE based on the latent heat of vaporization λ (positive temperatures) or sublimation (subzero temperatures), accounting for the slight dependence of λ on temperature.

NEE is computed as the sum of the EC flux at height z (F_c) and the rate of change of CO_2 storage in the air coumn below height z (S_c):

$$\mathrm{NEE} = F_c + S_c, \tag{10a}$$

where:

$$S_c = \int_0^z \rho_a \frac{dc}{dt} dz, \tag{10b}$$

ρ_a is the density of dry air (kg m^{-3}) and c is the CO_2 mixing ratio.

3.7.3 Eddy-covariance measurements at the BERMS sites

Eddy-covariance measurements of sensible and latent heat flux densities H and λE, net ecosystem exchange NEE, and the friction velocity u_* were made from twin scaffold towers at approximately twice the height of the forest canopy and 3 m from the surface at Fen. The measurements spanned Apr 1996 to Oct 2017 at OA, Apr 1999 to present at OBS, Aug 1999 to present at OJP, and 2003 to present at Fen, with gaps of June 2018 to July 2019 at OBS, Aug to Dec 2012 and Nov 2021 to June 2022 at OJP, and Dec 2010 to Dec 2012 at Fen.

Changes in EC instrumentation and processing software occurred over the study period (Fig. 2), with three configurations:

- the UBC BIOMET closed-path EC system and processing software, which was used for all years (1996 to 2017) at OA, 1999 to 2018 at OBS, and 1999 to 2012 at OJP;
- the LI-COR open-path (LI-7500) EC system with EddyPro (version 2) software (LI-COR Inc., Lincoln, NE, USA), which was deployed at Fen from 2003 to 2010;
- the LI-COR closed-path (LI-7200) EC system with EddyPro (versions 3 to 7) software (LI-COR Inc., Lincoln, NE, USA), which was deployed at OBS from 2019 to present, OJP from 2013 to present, and Fen from 2013 to present.

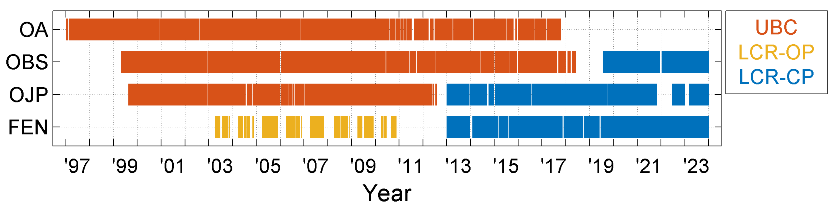

Figure 2. History of EC-system deployment at the BERMS sites, 1997-2023. White space indicates gaps of longer than one week. Legend: UBC – UBC closed-path EC system; LCR-OP – LI-COR LI-7500 open-path EC system; LCR-CP – LI-COR LI-7200 closed-path EC system.

The UBC BIOMET closed-path EC system consisted of a tri-axial sonic anemometer (model R2 (1997-1999) and R3 or R3-50 thereafter, Gill Instruments Ltd., Lymington, UK at OA and OBS; model CSAT3, Campbell Scientific Inc., Logan, UT, USA at OJP) in combination with a closed-path infrared (CO_2/H_2O) gas analyser (IRGA, model LI-6262

https://doi.org/10.5194/essd-2024-492
Preprint. Discussion started: 26 June 2025

or LI-7000, LI-COR Inc., Lincoln, NE, USA), operated in absolute mode. The fluxes were computed each half-hour from measurements at 20 Hz. The IRGA was enclosed in a temperature-controlled housing (UBC GA-TCH) that maintained the sample-cell temperature at 37 ± 0.5 °C. A diaphragm pump (model DOA-V191-AA, Gast Inc.) pulled air through a heated sampling tube (4 m length; 4 mm inner diameter) at flow rates of 10 L min^{-1} and 15 L min^{-1} for the LI-6262 and LI-7000 IRGAs, respectively (Krishnan et al., 2006; Barr et al., 2007, 2012). Daily calibrations to correct the CO_2 concentration measurements for zero and span shifts were implemented automatically using CO_2 standard gases from the Greenhouse Gases Measurement Laboratory (GGML) of Environment and Climate Change Canada in Downsview, ON, Canada (Krishnan et al., 2006). The IRGA reference cell was continuously flushed with dry nitrogen gas at a rate of 80 mL min^{-1}. The sample tubes were heated to prevent condensation and were replaced every 6-12 months to maintain the response times in H_2O and CO_2 sampling by minimizing the buildup of dust, pollen, and smoke particles on the tubing walls. Additional details are given in Black *et al.* (1996) and Zha et al. (2009).

The LI-COR open-path EC system consisted of a model LI-7500 IRGA (LI-COR Inc., Lincoln, NE, USA) with a model CSAT3 sonic anemometer (Campbell Scientific Inc., Logan, UT, USA), measured at 20 Hz and processed using EddyPro (LI-COR Inc., Lincoln, NE, USA). The LI-COR closed-path EC system consisted of a model LI-7200 IRGA (LI-COR Inc., Lincoln, NE, USA), with an unheated, insulated, stainless-steel inlet tube (5 mm ID, 0.65 m long at OBS and Fen; 8.5 mm ID, 1.04 m long at OJP), with a flow rate of 15 L min^{-1}; and a model CSAT3 sonic anemometer (Campbell Scientific Inc., Logan, UT, USA). The LI-COR closed-path data were measured at 10 Hz (OBS and OJP) or 20 Hz (Fen) and processed using EddyPro (LI-COR Inc., Lincoln, NE, USA). For both LI-COR open- and closed-path systems, the IRGA was calibrated manually 4 to 12 times each year.

The eddy-covariance energy storage flux terms S_H and $S_{\lambda E}$ (Eqs. 8b and 9b) were computed based the measured air temperature and humidity profiles at three or four levels per site (Section 3.1.1). The CO_2 storage flux S_c (Eq. 10b) was calculated either from the CO_2 concentration at a single level at the top of the tower as measured by the EC IRGA (for all years at Fen and after 2007 at the forest sites) or from a CO_2 concentration profile at eight levels as measured using a second IRGA (Yang et al., 1999). The profile system drew air continuously through each sample tube (Synflex 1300, 9.3 mm i.d.) at a flow rate of 25 L min^{-1} using a Gast model 1066 rotary pump. The inlet funnels were equipped with 7 µm (OJP) or 8 µm (OA and OBS) Nupro stainless steel filters and variable lengths of 4-mm i.d. Synflex tube to give the same pressure drop for all sampling tubes. The sampling tubes were sub-sampled sequentially at 6 L min^{-1} for 45s each using a Gast diaphragm pump, providing five measurements for each sampling height every half hour. After flushing the IRGA for 9 s, the CO_2 concentration was measured for 34 s. The five measurements per half-hour were then averaged to give the half-hourly mean at each height.

3.7.4 Minor surface-energy-balance terms

The soil heat flux Q_g was measured using four Middleton (Carter-Scott Design, Brunswick, Australia) model CN3 soil heat flux plates at 3-cm depth at SOA and 10-cm depth at the other sites, corrected for the heat storage change in the soil layer above the flux plates. At Fen, an additional term for heat storage in ponded water was added to Q_g. At the mature forest sites, the biomass heat storage flux Q_b was estimated from six to fifteen measurements of tree bole temperature using 30-gauge chromel-constantan thermocouples at several depths in the bole (McCaughey and Saxton

https://doi.org/10.5194/essd-2024-492
Preprint. Discussion started: 26 June 2025

1988, Blanken *et al.* 1997), using the biomass estimates of Gower *et al.* (1997). The photosynthetic energy flux Q_p was calculated from net ecosystem exchange (Blanken *et al.* 1997).

3.7.5 Data logging and telemetry

For periods processed with the UBC BIOMET EC software, the high-frequency data were processed on-site in real time, and the processed data uploaded once daily to UBC. The high frequency (20 Hz) data were stored on portable hard drives and shipped monthly to UBC, where the fluxes were reprocessed after any necessary calibration adjustments to the atmospheric CO_2 and H_2O mixing ratios. For periods processed with the EddyPro software, the high frequency data were also processed on-site in real time, and the processed data uploaded once daily to the Global Institute for Water Security in Saskatoon.

3.7.6 Quality assurance

Nighttime fluxes were rejected when u_* dropped below a site-specific u_* threshold u_*^{TH} (Goulden et al. 1996; Papale et al., 2006), as determined by change-point detection (Barr et al., 2013). One value was applied across all years: 0.35 m s^{-1} at OA, 0.30 m s^{-1} at OBS, 0.25 m s^{-1} at OJP, and 0.12 m s^{-1} at Fen). These values were based on the mean annual values early in the study periods, up to 2005, and were retained for consistency. An analysis of the stability of the u_*^{TH} over time is provided in Appendix C.

Flux data were also rejected based on automated and manual (graphical) outlier detection. For periods processed with the UBC BIOMET software, the flux data were screened using a dependency matrix, based on limit checking of the mean bench temperature, internal pressure, and pressure drop of the infrared gas analyzer, as well as the means and standard deviations of the CO_2 and H_2O mixing ratios and the three-dimensional components of the windspeed and air temperature of the ultrasonic anemometer. The exclusion criteria were conservative, so that only extreme outliers were flagged for exclusion. For periods processed using EddyPro, data were accepted when the Mauder and Foken (Foken et al., 2004) quality flag was 0 or 1 and rejected when it was 2. In addition, the NEE data were screened using the automated spike-detection method of Papale et al. (2006) using a spike-detection threshold of 7 s.d. from the mean, first based on the measured fluxes themselves then based on the difference between the measured fluxes and the corresponding modelled NEE estimate from the Fluxnet-Canada gap-filling procedure (Section 3.2.7).

3.7.8 Gap filling and partitioning EC fluxes

Gaps in the measured EC fluxes were filled annually. Gaps in H and λE were filled as described by Amiro et al. (2006). Briefly, simple empirical models were fit to the data using least-squares linear regression:

$$H = a_0(t) + a_1(t)\,(R_n - Q), \tag{11a}$$

$$\lambda E = b_0(t) + b_1(t)\frac{s}{(s+\gamma)}(R_n - Q), \tag{11b}$$

where s is the slope of the saturation vapor pressure curve (a function of T_a), γ is the psychrometric constant, and a_0, a_1, b_0, and b_1 are empirical parameters that vary over time t, estimated using a flexible moving window of 240 measured (not-missing) data points, moved in increments of 48 points at a time, with separate analyses for daytime and nighttime periods. The moving window normally spans 7-14 days, but may increase depending on the size and

https://doi.org/10.5194/essd-2024-492
Preprint. Discussion started: 26 June 2025

frequency of the data gaps. Eqs. (11a) and (11b) were used to fill gaps based on the independent measurements of R_n, Q, and T_a.

Gaps in NEE were filled and NEE was partitioned into R_e and GEP using the Fluxnet-Canada method (Barr *et al.*, 2004, Moffat et al. 2007). The infilling and partitioning were done annually. Briefly, R_e was estimated directly as R_e = NEE when GEP was known to be zero, i.e. at night and during the cold season (when either air or 5-cm soil temperature were 0 °C or less). An empirical $R_e = f(t, T_S)$ model was then fit to the measured R_e data, where T_S is soil temperature at the 5-cm depth; the model coefficients were allowed to vary over time t, and were fit using moving windows. For both R_e and GEP, the model coefficients were fit across a series of moving windows of 240 measured (not-missing) data points, moved in increments of 48 points. The model was used to fill gaps in R_e at night and during the cold season, and to estimate daytime R_e during the warm season. "Measured" GEP was then calculated from measured NEE and modeled R_e as R_e + (-NEE). Lastly, gaps in GEP were filled using an empirical light-response curve, with coefficients fit using moving windows. We also applied the marginal distribution sampling (MDS) method (Reichstein et al., 2005) for infilling NEE.

Random uncertainties in NEP, R_e and GEP were estimated following Richardson et al. (2006) using synthetic data from the Fluxnet-Canada gap-filling method (Barr et al., 2004).

3.7.9 Energy-balance closure

The surface energy balance (Eq. 4) may be written for measured fluxes with an additional error term ε:

$$R_n = H + \lambda E + Q + \varepsilon, \qquad (12)$$

where ε is the energy imbalance, a residual term that occurs when the sum of the EC sensible and latent heat fluxes ($H + \lambda E$) does not match the measured available energy ($R_n - Q$). The energy-closure fraction CF is defined as:

$$\mathrm{CF} = \frac{(H+\lambda E)}{(R_n - Q)}, \qquad (13)$$

where CF values below one indicate a flux measurement deficit.

The energy-closure fraction CF was computed annually from least-squares linear regression, forced through the origin, of 30-min H+λE versus R_n-Q. The analysis was limited to the warm season when all the energy-balance terms were measured. CF was then used to calculate an energy-closure adjusted value for evapotranspiration E^* as

$$E* = E/\mathrm{CF}, \qquad (14)$$

which forces energy balance closure while preserving the Bowen ratio ($H/\lambda E$) (Blanken et al. 1997, Twine et al. 2000, Wohlfahrt et al. 2010). Equation (11) was applied to all sites and years using an overall CF mean of 0.85 at the three forest sites, and values of 0.77 (up to 2012) and 0.68 (after 2012) at Fen. The CF values at Fen have high uncertainty because of the difficulties in estimating the ground heat flux, which includes ponded and moving water at this site.

4 Data Overview

4.1 Climate

The BERMS study area has a continental climate with a long, dry cold season and a short growing season. Based on the two sites (OBS and OJP) with complete measurements from 1997 to 2023, mean (± s.d.) annual air temperature

https://doi.org/10.5194/essd-2024-492
Preprint. Discussion started: 26 June 2025

Open Access Earth System Science Data Discussions

above the canopy was 1.4 ± 1.1 ºC. Monthly mean air temperature above the canopy ranged across years from -22.2 to -7.3 ºC in January (mean ± s.d. -15.7 ± 3.5 ºC) and 15.4 to 20.5 ºC in July (17.8 ± 1.2 ºC) (Fig. 3, left panel). The warmest years were 1998 (3.1 ºC), 2001 (2.9 ºC), and 2023 (2.9 ºC), with above-normal T_a in all seasons but winter 2023 (Fig. 4). The coldest years were 2014 (-0.2 ºC) related to a cold winter and cool spring, and 2004 (-0.2 ºC) related primarily to a cool spring and summer (Fig. 4).

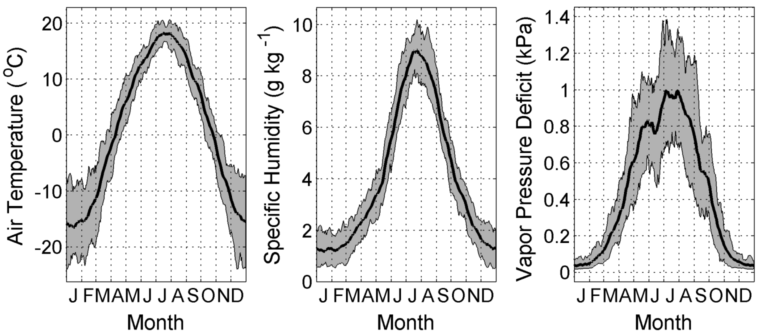

Figure 3. Annual cycles of mean daily above-canopy air temperature (left panel), specific humidity (middle panel) and vapor pressure deficit (right panel). The values are an average of the two continuously running sites (OBS and OJP), first smoothed as a 15-d running mean, then calculating the median (dark line) and 10th and 90th percentiles (lower and upper lines) across years.

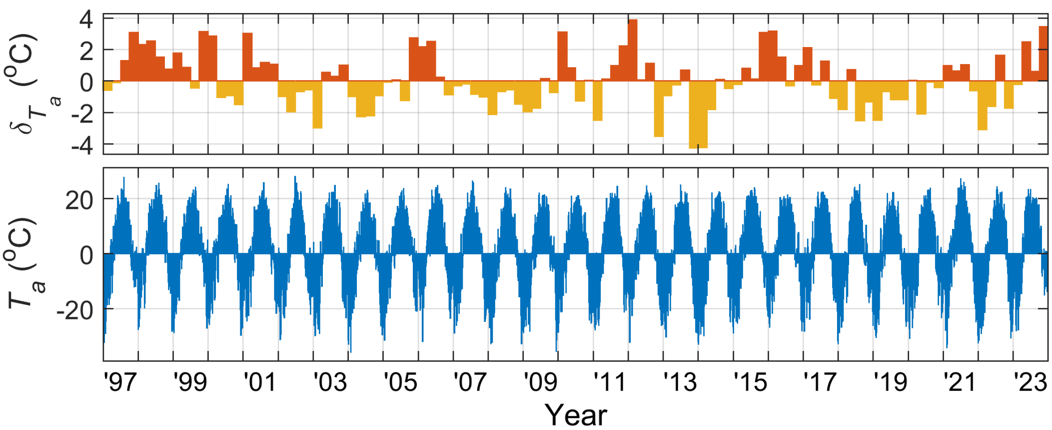

Figure 4. Mean daily above-canopy air temperature T_a (lower panel), averaged across the two sites (OBS and OJP) with complete data for 1997-2023, and its quarterly (three-month) anomaly δ_{Ta} (upper panel, green - positive anomalies; red – negative anomalies), computed as the departure from the long-term (1997-2023) mean quarterly (3-month) means.

Like air temperature, the annual cycles of specific humidity q and vapor pressure deficit VPD (Fig. 3, middle and right panels) peaked in July, but q rose later in spring and fell earlier autumn than T_a, related to the exponential dependence

https://doi.org/10.5194/essd-2024-492
Preprint. Discussion started: 26 June 2025

of the saturated vapor pressure on temperature. Unlike the smooth annual cycles of T_a and q, the annual VPD cycle plateaued in May-June with a secondary rise in late June, likely related to changes in surface energy partitioning with increasing soil water deficits in July and Aug. Monthly mean VPD was highest in July, ranging across years from 0.76 to 1.29 kPa (mean ± s.d. 0.97 ± 0.16 kPa). The anomaly in quarterly (three-month) mean VPD (δ_{VPD}, Fig. 5), computed as the departure from the long-term (1997-2023) quarterly mean, was positively correlated with the quarterly anomalies in T_a (δ_{Ta}, Fig. 4 upper panel) and incoming shortwave radiation $SW_{\downarrow}$ ($\delta_{SW\downarrow}$, Fig. 6 upper panel) but not wind speed (Fig. 7 upper panel), with correlation coefficients of 0.52 (δ_{VPD} vs δ_{Ta}, p <0.001) and 0.74 (δ_{VPD} vs $\delta_{SW\downarrow}$, p <0.001).

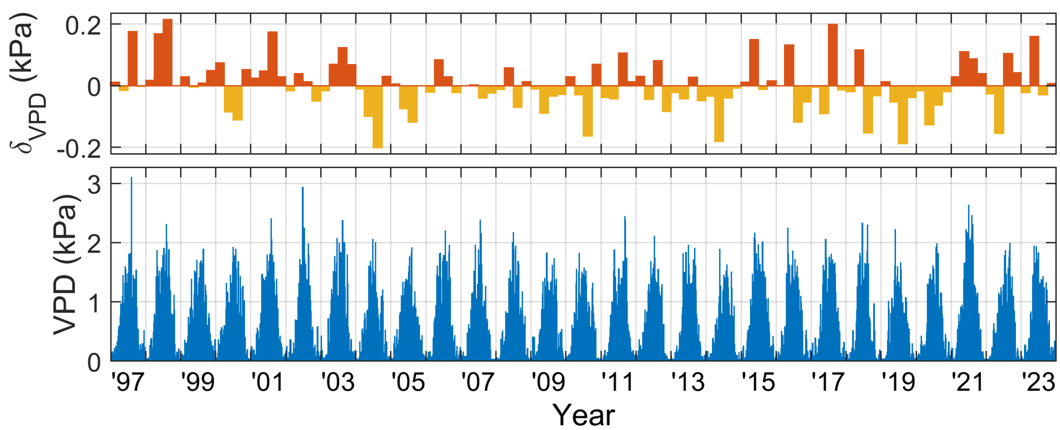

Figure 5. As Fig. 4 but for above-canopy vapor pressure deficit VPD, daytime values only.

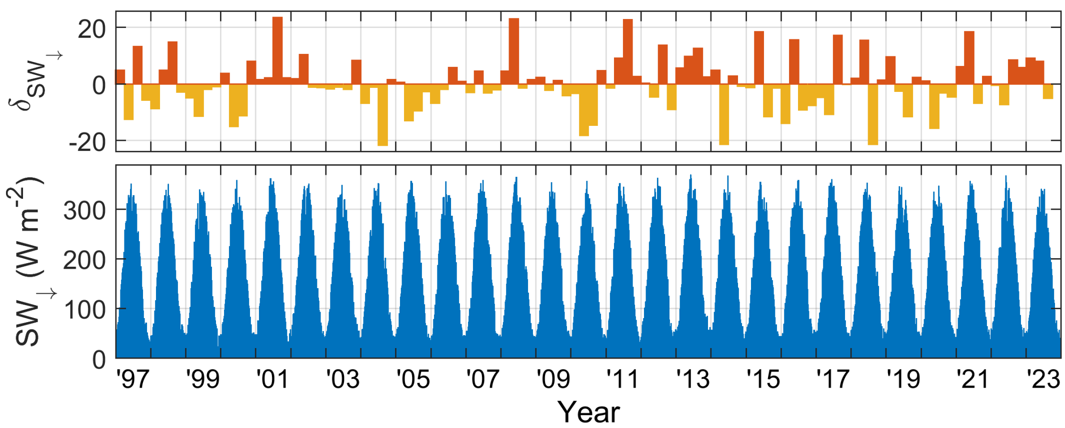

Figure 6. As Fig. 4 but for above-canopy, incoming shortwave radiation $SW_{\downarrow}$.

https://doi.org/10.5194/essd-2024-492
Preprint. Discussion started: 26 June 2025

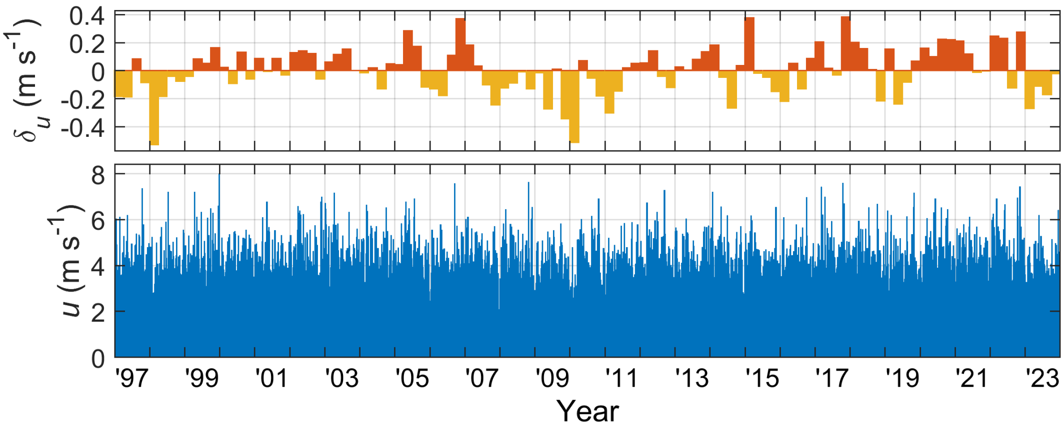

Figure 7. As Fig. 4 but for above-canopy wind speed *u*.

515

The annual cycles of soil temperature had the highest amplitude at OJP and Fen and the lowest amplitude at OBS (Fig. 8). February mean soil temperature at 10-cm depth (Table 3) was lowest at OJP and highest at Fen, with some years at Fen that did not freeze to 10-cm depth. July mean soil temperature at 10-cm depth was lowest at OBS and highest at Fen. The relatively buffered annual cycle of soil temperature at OBS was related to the insulating effect of its thick

520 feathermoss groundcover.

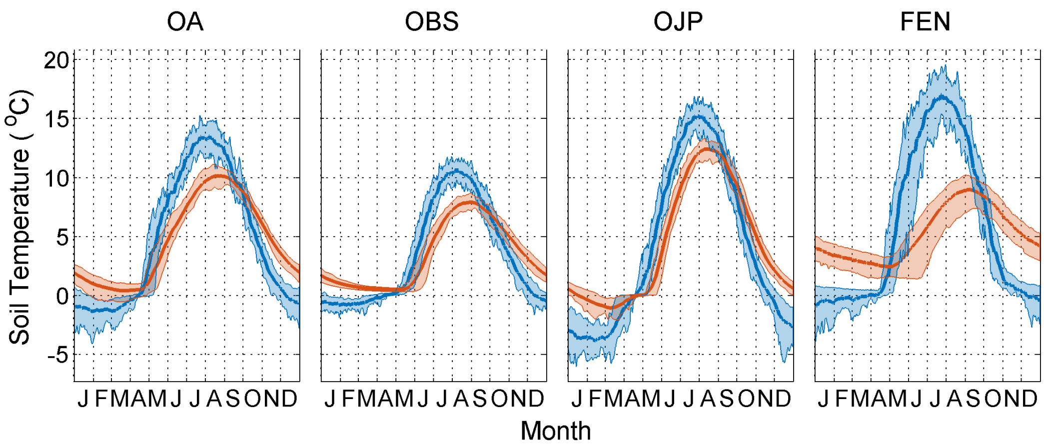

Figure 8. Annual cycles of soil temperature at the BERMS sites (blue: 10-cm depth, red: 100-cm depth). The values were first smoothed as daily means, then the median (dark lines) and 10th and 90th percentiles (lower and upper lines) were

525 **computed across years.**

Table 3. Mean monthly soil temperature at 10-cm depth at the BERMS sites, for the coldest (February) and warmest (July) months.

https://doi.org/10.5194/essd-2024-492
Preprint. Discussion started: 26 June 2025

		February		July	
		Mean (ºC)	Range (ºC)	Mean (ºC)	Range (ºC)
OA	1997-2017	-1.2 ± 0.9	-3.7 to -0.2	13.0 ± 0.7	11.6 to 14.3
OBS	1997-2023	-0.7 ± 0.3	-1.3 to -0.3	10.3 ± 0.5	9.2 to 11.3
OJP	1997-2023	-3.7 ± 0.8	-6.2 to -2.5	14.4 ± 0.8	12.6 to 15.5
Fen	2002-2023	-0.3 ± 1.0	-3.8 to +0.6	15.6 ± 1.2	13.5 to 17.8

Annual precipitation for the Oct-Sept hydrologic year ranged from a minimum of 236 mm at OA in 2001-2002 to a maximum of 645 mm at OBS in 2021-2022 with an overall mean (± s.d.) across sites of 489 ± 101 mm (Fig. 9). On average, 28% ± 7% of precipitation fell as snow, with annual snowfall totals ranging from 70 to 284 mm. Annual precipitation at OBS and OJP (1997-2023) showed three extended periods with contrasting dry, wet, and normal hydrologic regimes: 1997-2003 (406 ± 79 mm y^{-1}); 2004-2016 (555 ± 68 mm y^{-1}); and 2017-2023 (460 ± 85 mm y^{-1}). Related to the increased precipitation after 2003, annual streamflow from the White Gull watershed more than doubled from 69 ± 35 mm y^{-1} for 1994-2003 to 155 ± 56 mm y^{-1} for 2004-2022. To put these observations into an historic perspective, the long-term (1890-2012) climate observations from the nearby Prince Albert A show a 14% increase in annual precipitation between the pre-BERMS years (1890-1996) and years that overlap with BERMS (1997-2012), from 466 ± 99 mm y^{-1} to 528 ± 126 mm y^{-1}, respectively.

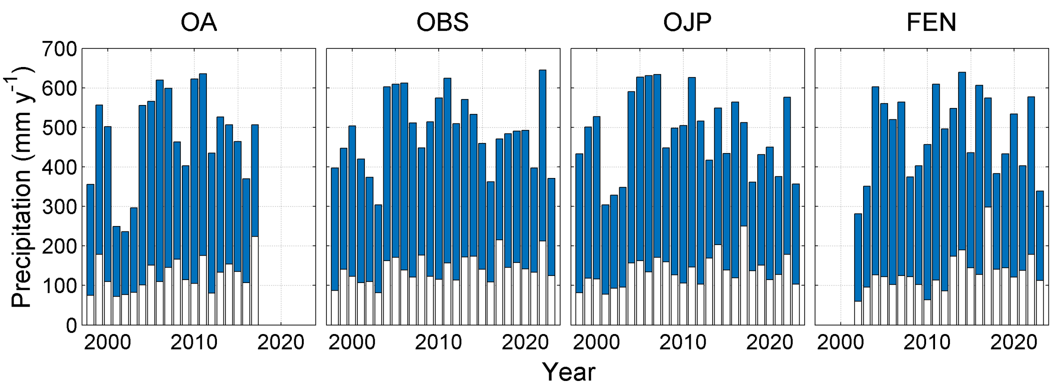

Figure 9. Annual precipitation over the Oct-Sept hydrologic year at the BERMS sites (level of the top of the blue bar), and its partitioning into rainfall (blue) and snowfall (white). The years on the x axis indicate the end of the hydrologic year.

4.2 Surface energy balance

The annual cycles of net radiation R_n and the sum of the minor surface-energy-balance terms Q were similar among sites, with the highest R_n values at OBS, followed by OJP, OA, and Fen (Fig. 10). The differences in R_n among sites

https://doi.org/10.5194/essd-2024-492
Preprint. Discussion started: 26 June 2025

arose primarily from differences in the shortwave albedo, with mean daily albedo values of 0.177 ± 0.046 (OBS), 0.223 ± 0.050 (OJP), 0.234 ± 0.052 (OA), and 0.807 ± 0.061 (Fen) in January and 0.081 ± 0.006 (OBS), 0.091 ± 0.005 (OJP), 0.145 ± 0.011 (OA), and 0.160 ± 0.014 (Fen) in July. For warm-season periods when the soil was thawed and our measurements of Q_g, Q_b, and Q_p comprised the entire surface-energy-storage flux Q, the ratio of Q to R_n, determined from least-squares linear regression forced through the origin, was 0.089 at OA, 0.063 at OBS, and 0.078 at OJP.

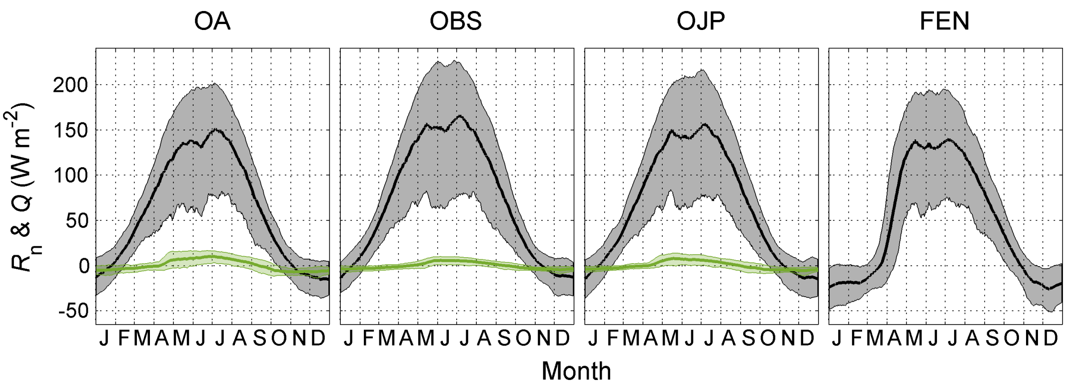

Figure 10. Annual cycles of 15-day running mean net radiation (grey) and the sum of the soil, biomass, and photosynthetic heat flux densities (green) at the BERMS sites, 1997-2022. The solid lines show the median annual cycle across years, and the upper and lower limits show the 10th and 90th percentiles.

The annual cycles of H and λE had striking differences among sites (Fig. 11). At all sites, mean daily H was slightly negative in Nov-Jan and increased rapidly to a seasonal maximum in May, whereas λE was near zero from Nov to Mar and reached a seasonal maximum in July. At the two evergreen needleleaf forests (OBS and OJP), H remained relatively high throughout the summer, with similar values to λE in August through Oct. At the deciduous broad leaf forest (OA), H declined rapidly and λE rose rapidly through the leafout period in May and June, and λE was the dominant term in summer. At Fen, λE exceeded H in every season. The mean (± s.d.) annual Bowen ratios ($H/\lambda E$) for the warm-season months of May to Sept were 0.43 ± 0.24 (OA), 0.98 ± 0.17 (OBS), 1.51 ± 0.23 (OJP), and 0.37 ± 0.08 (Fen).

https://doi.org/10.5194/essd-2024-492
Preprint. Discussion started: 26 June 2025

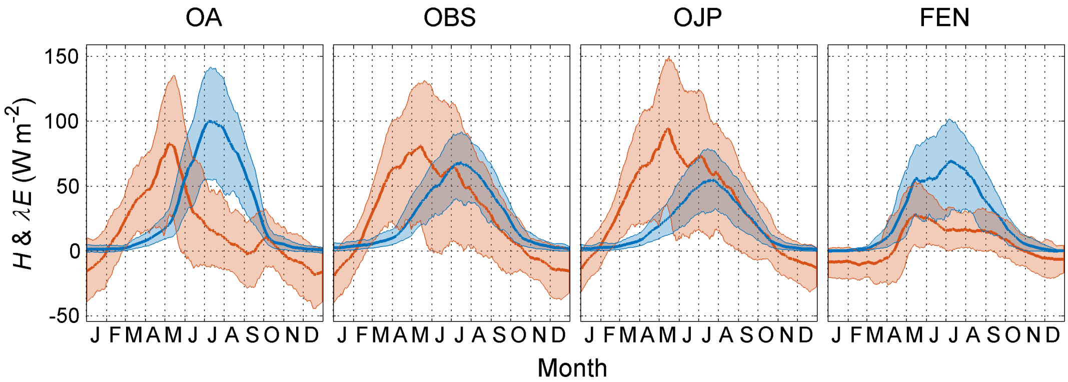

Figure 11. Annual cycles of the sensible (red) and latent (blue) heat flux densities (15-d running mean) at the BERMS sites. The solid lines show the median annual cycle across years, and the upper and lower limits show the 10th and 90th percentiles.

4.3 Vertical water balance

Mean annual P was similar among sites, but annual evapotranspiration E^* (after energy-balance-closure adjustment) varied from (mean ± s.d.) 292 ± 27 mm y^{-1} at OJP to 375 ± 31 mm y^{-1} at OBS, 443 ± 39 mm y^{-1} at Fen, and 448 ± 59 mm y^{-1} at OA (Fig. 12). The mean annual lateral outflow may be estimated as a residual term in the vertical water balance as $O = P - E^* - \Delta S$ (Eq. 2). Although ΔS can be large at an annual time scale, it becomes small when integrated over periods of decades, so that a long-term mean value of O may be estimated as $P - E^*$. The resulting long-term runoff ratios at the BERMS sites (O / P, estimated as (P- E^*) / P) are 8% at OA, 25% at OBS, 39% at OJP and 11% at Fen. The estimates for E^* and O are most uncertain at Fen because of high uncertainty in the energy-closure adjustment CF.

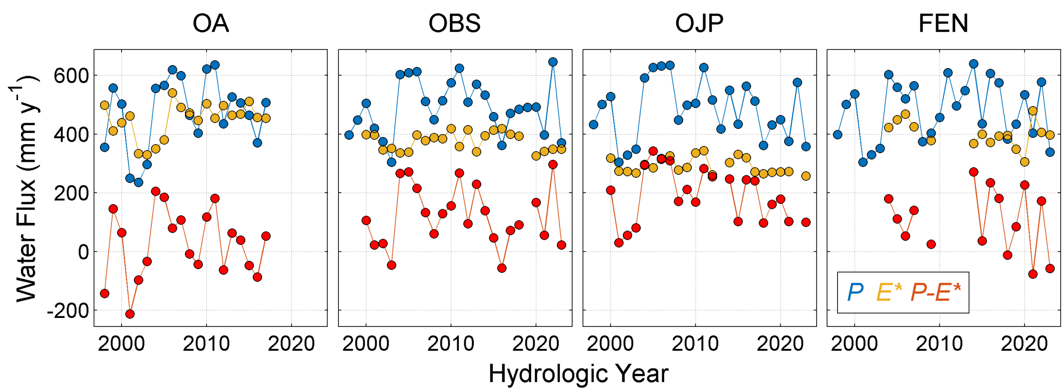

Figure 12. Annual precipitation *P*, evapotranspiration *E (after energy-balance-closure adjustment), and the difference *P*-*E** at the BERMS sites over the Oct-Sept hydrologic year, 1997-2023. The years on the x axis indicate the end of the hydrologic year.**

https://doi.org/10.5194/essd-2024-492
Preprint. Discussion started: 26 June 2025

4.4 Surface carbon balance

Like the sensible and latent heat fluxes, the annual cycles of net ecosystem production and its partition into gross ecosystem photosynthesis and ecosystem respiration had striking differences among sites (Figs. 13 and 14). The annual cycles of NEP and GEP were much more dynamic at OA than the other three sites. Over the annual cycle, all four sites have a relatively short period with mean positive C uptake, with the strongest C uptake from late May to mid Sept at OA, late Apr to early July at OBS and OJP, and June through Aug at Fen. During summer, OBS and OJP can be either a C sink or a C source. OA and Fen are moderate C sources in spring and fall, before leafout and after leaf senescence, when GEP is small but the soil is thawed and R_e is significantly above zero.

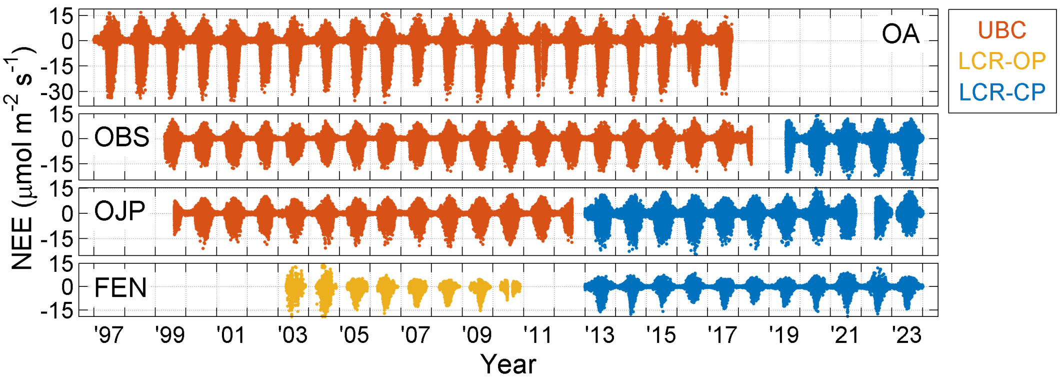

Figure 13. Half-hourly measurements of net ecosystem exchange NEE at the BERMS flux towers. Legend: UBC – UBC closed-path EC system; LCR-OP – LI-COR LI-7500 open-path EC system; LCR-CP – LI-COR LI-7200 closed-path EC system.

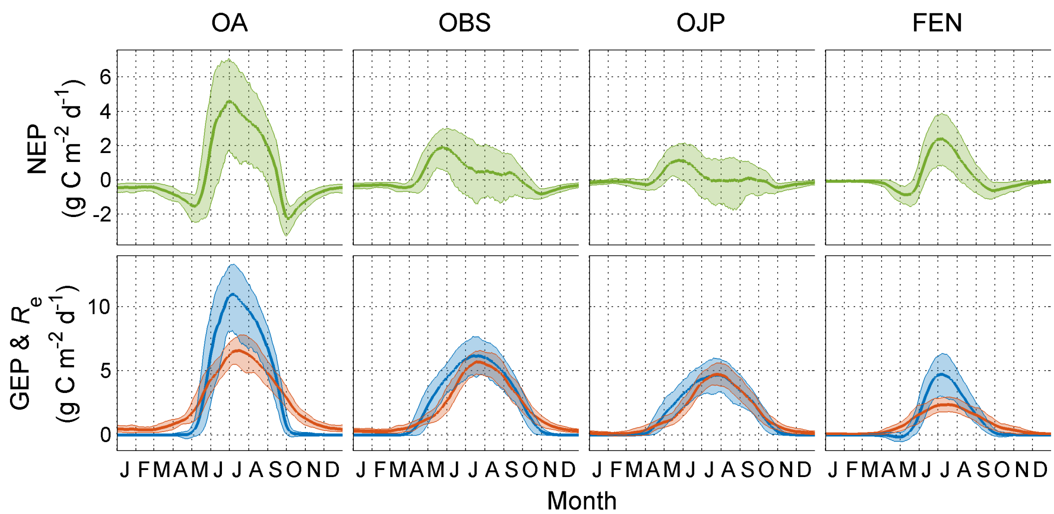

Figure 14. Annual cycles of net ecosystem production (upper panels) and its partition into gross ecosystem photosynthesis (blue) and ecosystem respiration (red) (lower panels) at the BERMS sites. The solid lines show the median annual cycle across years, and the upper and lower limits show the 10th and 90th percentiles. The values have been smoothed as 15-d running means.

On an annual basis (Fig. 15, Table 4), (mean ± s.d.) annual NEP = GEP - R_e were:

(128 ± 95) = (1053 ± 110) – (924 ± 79) g C m^{-2} y^{-1} at OA (1997-2017),

(51 ± 22) = (802 ± 51) – (751 ± 56) g C m^{-2} y^{-1} at OBS (2000-2017, 2019-2023),

(25 ± 35) = (606 ± 52) – (581 ± 54) g C m^{-2} y^{-1} at OJP (2000-2011, 2013-2023),

(16 ± 68) = (346 ± 65) – (329 ± 27) g C m^{-2} y^{-1} at Fen (2013-2023).

Note that both the mean fluxes and their inter-annual variability are higher at OA than the other sites. No significant temporal trends in annual NEP are evident except at OJP, where NEP declines rapidly in the years after 2012, switching from a weak C sink to a weak C source.

The values of annual NEP are atypical for three particular site-years: 2016 at OA, with annual NEP of -61 g C m^{-2} y^{-1} compared with 138 ± 86 g C m^{-2} y^{-1} for 1997-2015, related to low GEP that resulted from severe insect defoliation in June 2016 (Stephens et al., 2018); 2013 at Fen, with annual NEP of 175 g C m^{-2} y^{-1} compared with 3 ± 36 g C m^{-2} y^{-1} for 2014-2023, related to atypically high GEP for which the cause is unknown and which may be suspect; and 2023 at OJP, with annual NEP of -134 g C m^{-2} y^{-1} compared with 30 ± 28 g C m^{-2} y^{-1} for 2000-2020, related to atypically low GEP. The extremely low OJP-2023 NEP is consistent with a general decline that began in 2013, but the drop between 2020 and 2023 is extreme.

The pronounced declining trend in annual NEP at OJP after 2012 corresponds to a period of increased tree mortality, from less than 2% y^{-1} up to 2016 to 5% y^{-1} between 2016 and 2023 (Table 1), caused by increased windthrow. However, the post-2012 NEP decline at OJP also coincides with a change in the EC system, from the UBC EC system

https://doi.org/10.5194/essd-2024-492
Preprint. Discussion started: 26 June 2025

(up to 2012) to the LI-COR closed-path EC system in 2012. Appendix C explores the possible effect of the EC-system change on the measured fluxes. While the analysis is inconclusive and some causes for concern are identified, we found no compelling evidence that the EC-system changeover introduced a bias or discontinuity in annual NEP and believe that the declining NEP after 2012 at OJP is primarily related to increased tree mortality.

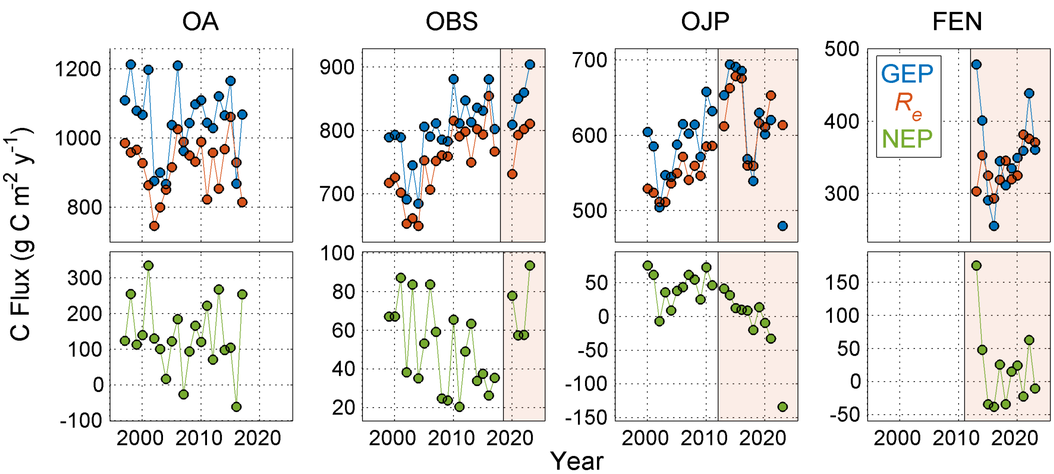

Figure 15. Annual net ecosystem production NEP (lower panel) and its partition into gross ecosystem photosynthesis GEP and ecosystem respiration Re (upper panel) at the BERMS sites. The unshaded and shaded areas show periods measured with the UBC and LI-COR closed-path EC systems, respectively. Note the difference in the y-axis scales for each site.

https://doi.org/10.5194/essd-2024-492
Preprint. Discussion started: 26 June 2025

Table 4 Annual C fluxes (NEP = GEP – R_e) (g C m^{-2} y^{-1}), with associated values of annual random uncertainty (g C m^{-2} y^{-1}) in brackets.

	OA	OBS	OJP	Fen
1997	123(44) = 1109(66) – 985(86)			
1998	254(48) = 1212(82) – 958(108)			
1999	113(44) = 1079(65) – 966(80)			
2000	139(39) = 1067(59) – 927(76)	67(27) = 793(44) – 726(61)	75(30) = 604(44) – 529(58)	
2001	334(44) = 1197(61) – 863(75)	87(31) = 789(57) – 702(75)	62(29) = 585(51) – 524(67)	
2002	130(40) = 876(51) – 746(59)	38(28) = 691(48) – 653(61)	-7(28) = 504(42) – 511(60)	
2003	100(34) = 900(48) – 800(60)	84(27) = 745(40) – 662(52)	36(27) = 547(36) – 511(50)	
2004	17(33) = 867(52) – 850(68)	35(26) = 685(45) – 650(59)	9(40) = 545(65) – 536(83)	
2005	122(35) = 1037(51) – 916(66)	53(27) = 806(47) – 753(61)	38(29) = 587(44) – 550(59)	
2006	184(41) = 1209(64) – 1025(86)	84(34) = 790(57) – 707(80)	43(45) = 615(84) – 571(118)	
2007	-26(37) = 962(57) – 989(72)	59(28) = 811(44) – 752(59)	62(29) = 602(43) – 541(62)	
2008	94(39) = 1043(55) – 949(68)	25(31) = 786(47) – 761(65)	55(33) = 614(52) – 559(71)	
2009	166(43) = 1097(65) – 932(85)	24(29) = 783(46) – 759(64)	25(35) = 571(50) – 546(72)	
2010	120(48) = 1109(73) – 989(92)	65(34) = 881(48) – 815(66)	73(36) = 658(61) – 585(81)	
2011	221(64) = 1044(71) – 822(82)	20(36) = 811(51) – 791(71)	46(31) = 632(48) – 586(63)	
2012	71(45) = 1028(63) – 958(76)	49(33) = 847(51) – 798(69)		
2013	267(39) = 1120(54) – 853(71)	63(30) = 813(45) – 750(60)	41(44) = 653(54) – 612(75)	175(25) = 478(39) – 303(56)
2014	98(41) = 1065(63) – 968(77)	34(38) = 836(62) – 802(87)	31(51) = 694(64) – 662(86)	48(20) = 401(29) – 353(40)
2015	104(49) = 1165(72) – 1061(93)	37(36) = 831(62) – 794(87)	12(42) = 691(59) – 678(80)	-34(25) = 291(39) – 325(58)
2016	-61(42) = 868(59) – 929(82)	26(34) = 881(56) – 854(73)	10(45) = 685(60) – 676(73)	-38(25) = 255(37) – 292(54)
2017		35(41) = 802(67) – 767(91)	9(35) = 568(45) – 560(60)	23(19) = 342(29) – 319(39)
2018			-20(33) = 539(42) – 559(51)	-34(19) = 307(29) – 347(41)
2019			14(40) = 630(53) – 616(75)	15(24) = 330(35) – 320(49)
2020		78(36) = 809(49) – 731(63)	-10(32) = 601(43) - 611(56)	24(19) = 349(25) - 325(35)
2021		57(41) = 850(66) – 793(84)	-33 = 620 – 653	-26(24) = 358(33) – 381(49)
2022		58(40) = 860(58) - 802(81)		59(20) = 433(28) - 374(39)
2023		93(39) = 904(59) - 810(76)	-134(46) = 480(47) - 613(74)	-10(22) = 361(35) - 371(50)
Mean	128(42) = 1053(61) – 924(77)	53(33) = 809(53) – 756(70)	22(36) = 600(52) – 578(70)	19(22) = 356(32) – 337(46)

In addition to our long-term use of the Fluxnet-Canada (FC) gap-filling method (Barr et al., 2004), we generated a second infilled NEP time series using the FLUXNET standard MDS method (Reichstein et al., 2005) (Fig. 16). Three observations from the MDS-FC comparison are noteworthy. First, the MDS and FC estimates of annual NEP are very highly correlated, with r values of or above 0.994 for all sites but OBS, which had r = 0.960 (Table 5). The high positive correlations indicate that the two methods show very similar patterns of interannual variability. Second, the MDS estimates of annual NEP are consistently higher than the FC estimates, with mean annual totals of: 140 (MDS) vs 128 (FC) g C m^{-2} y^{-1} at OA; 69 (MDS) vs 53 (FC) g C m^{-2} y^{-1} at OBS; 32 (MDS) vs 22 (FC) g C m^{-2} y^{-1} at OJP; and 23 (MDS) vs 19 (FC) g C m^{-2} y^{-1} at Fen (Fig. 16). Third, the MDS-FC differences in annual NEP are almost entirely

https://doi.org/10.5194/essd-2024-492
Preprint. Discussion started: 26 June 2025

due to the differences in the filling of nighttime gaps; the daytime means are nearly identical. Related to that observation, the MDS and FC estimates of annual daytime NEP are more strongly correlated (r of 0.987 to 1.000) than those of annual nighttime NEP (r of 0.953 to 0.985) (Table 5). Both FC and MDS methods performed well in the Moffat et al. (2007) intercomparison of NEE gap-filling methods; the difference between the two methods at the BERMS sites reflects the broader uncertainty in gap filling. We have not identified the cause of the day-night FC-MDS difference, nor do we know why the two methods diverge the most at OBS.

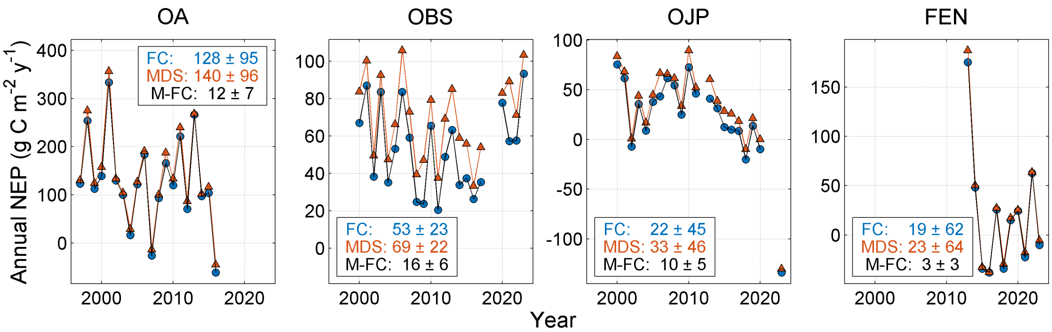

Figure 16. Comparison of Fluxnet-Canada (FC) and MDS gap-filled estimates of annual net ecosystem production NEP (g C m^{-2} y^{-1}) at the BERMS flux towers, 1997-2023. The values in the legend are the mean ± s.d. (g C m^{-2} y^{-1}) for both methods and the MDS-FC difference (M-FC). Years with data gaps of 2 months or longer have been excluded.

Table 5. Correlation coefficients comparing estimates of annual net ecosystem production NEP from the Fluxnet-Canada (FC) and MDS gap-filling methods at the BERMS flux towers, 1997-2023. Also shown are the MDS vs FC correlation coefficients for annual total daytime and nighttime NEP.

	OA	**OBS**	**OJP**	**Fen**
Annual	0.998	0.960	0.994	0.999
Daytime	1.000	0.987	0.994	1.000
Nighttime	0.984	0.970	0.985	0.953

5 Evaluation and Known Issues

5.1 Eddy-covariance fluxes

We evaluated the long-term stability of the eddy-covariance measurements based on annual analyses of energy-balance closure (Section 3.2.8, Appendix C), the computed u_*^{TH} filter (Section 3.2.6, Appendix C), and the random uncertainty in NEE (Section 3.2.7, Appendix C). The annual energy-closure fraction CF at the forest sites, based on daytime, warm-season periods only, was relatively consistent among sites and years but dropped slightly in the later years. The mean annual CF was 0.84 ± 0.05 (OA), 0.82 ± 0.04 (OBS), and 0.84 ± 0.03 (OJP) (Appendix C, Fig. C1, left panel). The annual estimates of u_*^{TH} were extremely well defined at OA and OBS, well defined at OJP, and poorly defined at Fen (Appendix C, Fig. C2). Annual u_*^{TH} evaluation at the forest sites showed positive trends at OA and

https://doi.org/10.5194/essd-2024-492
Preprint. Discussion started: 26 June 2025

OBS (up to 2018, over the years with the UBC EC system) but no trend at OJP. Random uncertainty in annual NEP, GEP and R_e, as evaluated using the Richardson-Hollinger method (Section 3.2.9) varied among sites but was mostly stable over the period of measurement at each site (Appendix C, Fig. C4). The random uncertainty in annual GEP averaged 6%, 7%, 9% and 9% of annual mean GEP at OA, OBS, OJP, and Fen, respectively, compared to 8%, 9%, 12% and 14% of mean annual R_e. The random uncertainty in NEP, although smaller than that of GEP and R_e, was large when compared to mean annual NEP, with mean values of 42 versus 128 g C m^{-2} y^{-1}, respectively, at OA, 33 versus 53 g C m^{-2} y^{-1} at OBS, 36 versus 22 g C m^{-2} y^{-1} at OJP, and 22 versus 19 g C m^{-2} y^{-1} at Fen. The NEP random uncertainty showed no clear temporal trends at OA and Fen but rose at OBS and OJP, in part associated with the changeover from the UBC to the LI-COR closed-path EC system (Appendix C, Fig. C4).

At OJP and OBS, a number of differences in the flux data before and after the EC-system changeovers raised questions about the continuity of the flux time series, although we found no conclusive evidence that the change had introduced bias. Complete EC-system replacements took place at OJP and Fen in 2012 and at OBS in 2018 (Section 3.2.3). At Fen, the replacement of the LI-COR open-path with the LI-COR closed-path EC system resulted in the first year-round flux measurements in 2013; prior to 2012, only warm-season fluxes could be measured, which excluded 4-5 months each winter. At both OBS and OJP, annually-derived estimates of u_*^{TH} were similar before and after the EC-system changeovers (from the UBC to the LI-COR open-path EC instrumentation and software), however the changeovers increased random noise in NEE at both sites (Appendix C, Fig. C5), resulting in a mean increase in the random uncertainty in annual NEP from 32 to 39 g C m^{-2} y^{-1} at OBS and 33 to 41 g C m^{-2} y^{-1} at OJP (Appendix C, Fig. C4). At OJP, mean annual CF was slightly higher for measurement years with the UBC (0.86 ± 0.02) than the LI-COR open-path (0.82 ± 0.02) EC system and software, however, no CF difference was found between the two EC systems at OBS (Appendix C, Fig. C1). Perhaps most problematically, the changeover from the UBC to the LI-COR closed-path EC system introduced a marked discontinuity in cold-season NEE at both OBS and OJP, with anomalously-low daytime NEE values from the LI-COR system at both sites, and many values that were implausibly below zero at OJP (Appendix C, Figs. C6 and C7). See Appendix C for further details.

5.2 Meteorological and soil variables

In general, most meteorological and soil state-variable measurements were stable over time, with no observed drift or discontinuities. The three main exceptions are: PPFD, whose sensors should have been recalibrated annually as the sensors aged beyond ~ 5 years (Korde and Geist, 1987); relative humidity, which has several gaps of one to four years due to sensor malfunction; and soil VWC, where discontinuities were introduced by sensor failure or relocation at particular depths and sites only. The PPFD sensors have not been recalibrated since they were last replaced in ~ 2007. For sensors measuring above-canopy, outgoing PPFD and those measuring incoming below-canopy PPFD, the lack of ongoing calibration introduces an unknown and uncorrected bias after 2012. For sensors measuring above-canopy incoming PPFD (PPFD$_{\downarrow}$), however, an annual, in-situ calibration was possible in relation to above-canopy, incoming shortwave radiation SW$_{\downarrow}$, based on our conclusion that the SW$_{\downarrow}$ sensors were stable over time and that the mean annual clear-sky PPFD$_{\downarrow}$/ SW$_{\downarrow}$ ratio was constant (Appendix D). Relative to SW$_{\downarrow}$, our analysis shows that the decline in measured above-canopy PPFD$_{\downarrow}$ began after 2011 and was gradual, well-defined, and totaled about 20% by 2022.

https://doi.org/10.5194/essd-2024-492
Preprint. Discussion started: 26 June 2025

Open Access Earth System Science Data Discussions

Based on the observed decline in the annual PPFD$_{\downarrow}$/ SW$_{\downarrow}$ ratio, we used an annual, in-situ calibration to recompute PPFD$_{\downarrow}$ after 2011. See Appendix D for further details.

Above-canopy relative humidity has two long gaps: Oct 2013 to Dec 2017 at OA and Oct 2014 to Dec 2018 at OBS. Two of the within-canopy relative humidity time series at OA also have shorter gaps of 19 and 30 months at the end of the time series. The data gaps at OA are related to much-reduced sensor servicing after 2012. The gaps have been infilled as described in Appendix B, based on relationships with related time series from the same or nearby sites over the preceding years. The infilled data, although limited in utility, appear credible and should be adequate as drivers in modelling studies.

Instabilities in soil VWC were more difficult to resolve. At OA, the VWC measurement location and instrumentation were changed in 2007, when flooding at the original, low-lying location made it necessary to relocate the measurement to a slightly higher elevation that was more typical of the flux-tower footprint. The change resulted in a discontinuity in the VWC time series at all depths in 2007-2008. At the other sites, the failure of some sensors over the 27-year measurement span resulted in discontinuities in VWC, with 4 of the 12 original sensors failing at OJP, 6 of 10 sensors failing at OBS. Because of the severity of the issues at OBS, the 2.5, 22.5 and 60-90 cm VWC depths have been excluded from the archive. Details are given in Appendix D. No site-specific calibrations were applied to any of the soil VWC measurements. Our attempts at field validation, while not definitive, resulted in the greatest confidence in the absolute accuracy of the measured VWC at OJP followed by OA, related to the sandy soil at OJP and the use of true TDR at OA. We are less confident in the absolute values of the measured VWC at OBS and Fen, where the measurements at 0-30 cm depths were in organic soil layers which typically require calibration.

In addition, data users should note that a few winter measurements were affected by snow, hoar frost, or freeze-thaw processes, and that the archived data have not been screened to eliminate the questionable periods. Care should be exercised when using the cold-season values of incoming, below canopy PPFD, which was unventilated and subject to periods of snow or hoar frost on the sensor; soil VWC, which is reported year-round but only measures total soil water content when the soil is not frozen; and soil heat flux and biomass heat storage flux, which are reported year-round but are only meaningful during periods when there is no snowpack and the soil and tree boles are not frozen.

6 Data Availability

The BERMS data set, as described in this paper, are archived at the Federated Research Data Repository of the Digital Research Alliance of Canada and are freely available at https://doi.org/10.20383/103.01318 (Helgason et al., 2024).

7 Code Availability

The Matlab code used to process the data described in this manuscript is included within the data archive https://doi.org/10.20383/103.01318 (Helgason et al., 2024).

https://doi.org/10.5194/essd-2024-492
Preprint. Discussion started: 26 June 2025

Open Access Earth System Science Data Discussions

8 Conclusions

This paper describes the 1997-2023 meteorological and eddy-covariance flux data from the four long-term Boreal Ecosystem Research and Monitoring Sites (BERMS) in central Saskatchewan Canada. Among the boreal forest sites in the worldwide network of flux-tower research sites, the BERMS dataset is one of the longest and best. The 30-min data include meteorological variables (air temperature and humidity, barometric pressure, wind speed and direction, and precipitation), soil temperature and water content, the radiation balance (net, incoming and outgoing short- and longwave, incoming and outgoing PPFD), the surface energy balance (net radiation, latent and sensible heat fluxes, soil heat flux, biomass heat storage flux, and photosynthetic energy flux), and the surface carbon balance (net ecosystem production and its partition into gross ecosystem photosynthesis and ecosystem respiration). The strengths of the data set are its length and completeness, spanning up to 25 years; the care given to the measurement of net radiation and the minor surface energy balance terms; the care given to the measurement of precipitation and other hydrologic variables; and the proximity of the sites, which enables inter-site comparisons of the responses of the carbon and water balances to climatic controls.

https://doi.org/10.5194/essd-2024-492
Preprint. Discussion started: 26 June 2025

Appendix A Instrumentation History at BERMS

The history of the primary instruments deployed at the BERMS sites, 1997-2023, is summarized in Tables A1 (meteorology), A2 (soil temperature and water content), and A3 (eddy-covariance fluxes).

760 **Table A1 Long-term meteorological instrumentation**

Site	Variable (Unit)	Height (m)	Instrumentation	Data Period*
OA	Air Temperature (ºC)	1, 4, 18, 37	Vaisala HMP35CF *	1997 to July 2001
			Vaisala HMP45C *	July 2001 to 2017
			Type-K 40-gauge thermocouple	Nov 2004 to 2017
	Relative Humidity (%)	1, 4, 18, 37	Vaisala HMP35CF	1997 to July 2001
			Vaisala HMP45C	July 2001 to 2017
	Wind Speed (m s^{-1})	38	RM Young 05103	1997 to 2017
	Incoming Shortwave Radiation (W m^{-2})	37	Kipp & Zonen CM11 *	1997 to 2017
			Kipp & Zonen CNR1	2003 to 2017
	Outgoing Shortwave Radiation (W m^{-2})	31	Kipp & Zonen CM11 *	1997 to 2017
			Kipp & Zonen CNR1	2003 to 2017
	Incoming Longwave Radiation (W m^{-2})	37	Eppley PIR *	1997 to 2016
			Kipp & Zonen CNR1	2003 to 2017
	Outgoing Longwave Radiation (W m^{-2})	31	Eppley PIR *	1997 to 2017
			Kipp & Zonen CNR1	2003 to 2017
	Incoming PPFD (µmol m^{-2} s^{-1})	4, 37	LI-COR LI-190	1997 to 2017
	Outgoing PPFD (µmol m^{-2} s^{-1})	31	LI-COR LI-190	1997 to 2017
	Barometric Pressure (kPa)	2 *(in hut)*	Setra SBP270	1997 to 2017
	Precipitation (mm)	3	Belfort 3000	1997 to 2016
	Rainfall (mm)	2.5	Texas Electronics TE525	1997 to Sept 2002
			Hydrological Services TB3	Sept 2002 to 2016
OBS	Air Temperature (ºC)	1, 6, 25	Vaisala HMP35CF	1997 to June 2002
			Vaisala HMP45C	June 2002 to 2023
			Type-K 40-gauge thermocouple	Oct 1998 to 2023
	Relative Humidity (%)	1, 6, 25	Vaisala HMP35CF	1997 to June 2002

https://doi.org/10.5194/essd-2024-492
Preprint. Discussion started: 26 June 2025

			Vaisala HMP45C	June 2002 to 2023
	Wind Speed (m s^{-1})	26	RM Young 05103	1997 to 2023
	Incoming Shortwave Radiation (W m^{-2})	25	Kipp & Zonen CM11	1997 to 2023
	Outgoing Shortwave Radiation (W m^{-2})	20	Kipp & Zonen CM11	1997 to 2023
	Incoming Longwave Radiation (W m^{-2})	25	Eppley PIR *	1997 to 2023
		20	Kipp & Zonen CNR1	2007 to 2023
	Outgoing Longwave Radiation (W m^{-2})	25	Eppley PIR *	1997 to 2023
		20	Kipp & Zonen CNR1	2007 to 2023
	Incoming PPFD (µmol m^{-2} s^{-1})	1, 25	LI-COR LI-190	1997 to 2023
	Outgoing PPFD (µmol m^{-2} s^{-1})	20	LI-COR LI-190	1997 to 2023
	Barometric Pressure (kPa)	2 *(in hut)*	Setra SBP270	1997 to 2023
	Precipitation (mm)	5	Belfort 3000	1997 to 2011
		5 (2) **	Geonor T-200B	2012 to 2023
	Rainfall (mm)	5 (1) +	Texas Electronics TE525	1997 to Aug 2022
			Hydrological Services TB3	Aug 2022 to 2023
OJP	Air Temperature (ºC)	1, 10, 28	Vaisala HMP35CF *	1997 to Dec 2001
			Vaisala HMP45C *	Dec 2001 to 2023
			Type-K 40-gauge thermocouple	1997 to 2023
	Relative Humidity (%)	1, 10, 28	Vaisala HMP35CF	1997 to Dec 2001
			Vaisala HMP45C	Dec 2001 to 2023
	Wind Speed (m s^{-1})	29	RM Young 05103	1997 to 2023
	Incoming Shortwave Radiation (W m^{-2})	28	Kipp & Zonen CM11	1997 to Sept 2010
			Kipp & Zonen CMP11 *	Sept 2010 to 2023
			Kipp & Zonen CNR1	Sept 2010 to 2023
	Outgoing Shortwave Radiation (W m^{-2})	23	Kipp & Zonen CM11	1997 to Sept 2010
			Kipp & Zonen CMP11 *	Sept 2010 to 2023
			Kipp & Zonen CNR1	Sept 2010 to 2023
	Incoming Longwave Radiation (W m^{-2})	28	Eppley PIR	1997 to Sept 2013
			Kipp & Zonen CGR4 *	Oct 2010 to 2023
			Kipp & Zonen CNR1	Sept 2010 to 2023

	Outgoing Longwave Radiation (W m^{-2})	23	Eppley PIR	1997 to Sept 2013
			Kipp & Zonen CGR4 *	Oct 2010 to 2023
			Kipp & Zonen CNR1	Sept 2010 to 2023
	Incoming PPFD (µmol m^{-2} s^{-1})	1, 28	LI-COR LI-190	1997 to 2023
	Outgoing PPFD (µmol m^{-2} s^{-1})	23	LI-COR LI-190	1997 to 2023
	Barometric Pressure (kPa)	2 *(in hut)*	Setra SBP270	1997 to 2023
	Precipitation (mm)	3	Belfort 3000	1997 to Sept 2010
		2	Geonor T-200B	Sept 2010 to 2023
	Rainfall (mm)	2.5	Texas Electronics TE525	1997 to Aug 2002
			Hydrological Services TB3	Aug 2002 to 2023
FEN	Air Temperature (°C)	2, 15	Vaisala HMP45C	2002 to Jul 2023
			Vaisala HMP155A	Jul to Dec 2023
		4, 8	Vaisala HMP45C	2002 to Jul 2023
	Relative Humidity (%)	2, 15	Vaisala HMP45C	2002 to Jul 2023
			Vaisala HMP155A	Jul to Dec 2023
		4, 8	Vaisala HMP45C	2002 to Jul 2023
	Wind Speed (m s^{-1})	15	RM Young 05103	2002 to 2023
	Incoming Shortwave Radiation (W m^{-2})	15	Kipp & Zonen CNR1	2003 to Nov 2014
			Kipp & Zonen CNR4 ++	Nov 2014 to 2023
	Outgoing Shortwave Radiation (W m^{-2})	15	Kipp & Zonen CNR1	2003 to Nov 2014
			Kipp & Zonen CNR4 ++	Nov 2014 to 2023
	Incoming Longwave Radiation (W m^{-2})	15	Kipp & Zonen CNR1	2003 to Nov 2014
			Kipp & Zonen CNR4 ++	Nov 2014 to 2023
	Outgoing Longwave Radiation (W m^{-2})	15	Kipp & Zonen CNR1	2003 to Nov 2014
			Kipp & Zonen CNR4 ++	Nov 2014 to 2023
	Incoming PPFD (µmol m^{-2} s^{-1})	15	LI-COR LI-190	2003 to 2023
	Outgoing PPFD (µmol m^{-2} s^{-1})	15	LI-COR LI-190	2003 to 2023
	Barometric Pressure (kPa)	2 *(in hut)*	Vaisala PTA427A	2011 to 2023
	Precipitation (mm)	2	Belfort 3000	2002 to 2010
		5 (2) **	Geonor T-200B	2011 to 2023

https://doi.org/10.5194/essd-2024-492
Preprint. Discussion started: 26 June 2025

Rainfall (mm)	1	Texas Electronics TE525 Hydrological Services TB3	2002 to May 2021 May 2021 to 2023

* when variables were measured redundantly, the primary instrument is indicated

** Geonor T-200B moved from the roof of the hut to ground level in May 2023

+ TB3 rain gauge moved from roof of hut to ground level in May 2023

++ CNR4 removed for repairs July 2019 and replaced with CNR1; CNR4 redeployed July 2023

Table A2 Long-term instrumentation for soil temperature and volumetric water content

Site	Variable (Unit)	Instrumentation	Depths (cm)	Data Period*
OA	Soil Temp (ºC)	Type-T thermocouples	2, 5, 10, 20, 50,100	1997 to 2017
	Soil VWC (m³/m³)	CS615 reflectometers	2.5 and 7.5	1997 to 2017
		Moisture Point Type-B TDR probes	0-15, 15-30, 30-60, 60-90, 90-120	1997 to 2008
		Campbell TDR-100	2.5, 7.5, 0-15, 15-30, 30-60, 60-90, 90-120	2007 to 2017
OBS	Soil Temp (ºC)	Type-T thermocouples	2, 5, 10, 20, 50,100	1997 to 2023
	Soil VWC (m³/m³)	CS615 reflectometers	7.5, 22.5	1997 to 2023
OJP	Soil Temp (ºC)	Type-T thermocouples	2, 5, 10, 20, 50,100	1997 to 2023
	Soil VWC (m³/m³)	CS615 reflectometers	0-15, 15-30, 30-60, 60-90, 90-120, 120-150	1997 to 2023
		CS616 reflectometers	0-15	2013 to 2023
Fen	Soil Temp (ºC)	Type-T thermocouples	2, 5, 10, 20, 50,100	2003 to 2023
	Soil VWC (m³/m³)	CS616 reflectometers	0-15 and 15-30	2004 to 2023

https://doi.org/10.5194/essd-2024-492
Preprint. Discussion started: 26 June 2025

Open Access Earth System Science Data Discussions

Table A3: Eddy-covariance (EC) measurements

	OA	OBS	OJP	Fen
Sonic anemometer	Gill R2 (*1997-1999*) Gill R3 or R3-50 (*2000-2017*)	Gill R2 (*1997-1999*) Gill R3 or R3-50 (*2000-2017*) CSAT3 (2018-2023)	CSAT3	CSAT3
IRGA	LI-6262 *(1997 - 2005)* LI-7000 *(2005 - 2017)*	LI-6262 *(1999 - 2007)* LI-7000 *(2007 - 2018)* LI-7200 *(2019 - 2023)*	LI-6262 *(1997 - 2012)* LI-7200 *(2012 - 2023)*	LI-7500 *(2002 - 2012)* LI-7200 *(2012 - 2023)*
EC height (m) [a]	39	25	29	2.5
Fetch[a]	3 km in all directions	>1.5 km in all directions, most uniform to 300 m	>1 km in all directions	125 m to east >500 m to north, south & west
Unstable flux footprint (m)[b]	450–550	200–300	250–400	
Neutral to stable flux footprint (m)[b]	900	500	600	

[a] Barr et al. (2006)

https://doi.org/10.5194/essd-2024-492
Preprint. Discussion started: 26 June 2025

Open Access Earth System Science Data Discussions

Appendix B Filling Gaps in Meteorological Data

The approaches used for infilling missing meteorological data are described in Table B1. The preferred gap-filling methods vary with the length of the data gap, and to a lesser extent, with the variable type.

Table B1 Methods used to fill gaps in meteorological time series, where *y* is the time series with missing values to be infilled, *x* is a closely-related, highly-correlated time series with non-missing values over the gaps in *y*, and $y^F(t)$ are the infilled values.

Infilling Method	Description	Gap Size	Variables*
Linear Interpolation	Linear interpolation over gap in *y*, does not require related *x* time series	gap ≤ 2h	All except precipitation
Interpolated Difference	Missing *y* infilled as $y^F(t) = x(t) + \Delta(t)$ where *x* is a closely related time series and $\Delta(t) = y(t) - x(t)$ is the interpolated difference across the gap in *y*	2 h < gap ≤ 12 h	T_a, RH, q, P, $LW_{\downarrow}$, $LW_{\uparrow}$, R_n, T_s, VWC
Moving-Window Linear Regression by Time of Year	Least-squares regression $y^F(t) = a_0 + a_1x(t)$ ** with parameter fitting using a temporal moving window of 240 non-missing (*x*,*y*) pairs	12 h < gap ≤ 3 months	RH, q, P, T_s (50,100 cm), VWC
Moving-Window Linear Regression by Time of Year and Time of Day	Least-squares regression $y^F(t) = a_0 + a_1x(t)$ ** with parameter fitting by time of day (e.g., separately for 0030, 0100, … 2400) using a temporal moving window of 30 non-missing (*x*,*y*) pairs	2 h < gap ≤ 3 months	$LW_{\downarrow}$, $LW_{\uparrow}$ $a_0 = 0$: u, $SW_{\downarrow}$, $SW_{\uparrow}$, $PPFD_{\downarrow}$, $PPFD_{\uparrow}$**
		12 h < gap ≤ 3 months	T_a, T_s (2-20 cm), R_n
Moving-Window Linear Regression based on same time of year over previous 5 years	Least-squares regression $y^F(t) = a_0 + a_1x(t)$ with parameter fitting using a 28-day moving window pooling data by time of year from the previous 5 years	Gap > 3 months	RH, q, P, T_s, VWC
Moving-Window Linear regression based on same time of year and time of day over previous 5 years	Least-squares regression $y^F(t) = a_0 + a_1x(t)$ with parameter fitting using a 28-day moving window pooling data by time of year and time of day from the previous 5 years	Gap > 3 months	T_a, $LW_{\downarrow}$, $LW_{\uparrow}$, R_n $a_0 = 0$: u, $SW_{\downarrow}$, $SW_{\uparrow}$, $PPFD_{\downarrow}$, $PPFD_{\uparrow}$,
Direct replacement, with scaling	$y^F(t) = x(t)$ if the total accumulation over then data gap is unknown;	All gap sizes	Interval precipitation

	$y^F(t) = cx(t)$ if the total accumulation across the data gap is known; c is computed separately for each data gap as the ratio of the total accumulations of y and x.		

* T_a air temperature; RH relative humidity; q specific humidity; P barometric pressure; u windspeed; $SW_{\downarrow}$, $SW_{\uparrow}$ incoming and outgoing shortwave radiation; $LW_{\downarrow}$; $LW_{\uparrow}$ incoming and outgoing longwave radiation; $PPFD_{\downarrow}$ $PPFD_{\uparrow}$; incoming and outgoing photosynthetically-active photon flux density; T_s soil temperature; VWC soil volumetric water content.

** when $a_0 = 0$, the regression line is forced through the origin

Identifying the preferred infilling method

The selection of infilling methods (Table B1) was based on extensive testing across eight gap sizes from 2 h to 1 yr. The evaluation randomly excluded 1% of the known values using a Monte-Carlo process, then infilled the gaps using each method. The procedure was applied annually over a 20-year period (1998-2016), with 50 repetitions. The best infilling method for each gap size and variable type was identified based on the lowest mean absolute error.

The best infilling method varied with gap size and variable, although many commonalities were found among variables. Overall, gaps of 2h or less were best filled by simple linear interpolation, whereas gaps of more than 2h were best filled based on statistical relationships with a closely-related (highly-correlated) time series from the same or a nearby site: gaps of 8 h by interpolated difference, gaps of one day to one month using moving-window linear regression sometimes limited to the same time of day, and gaps of 3 months to 1 year using moving-window regression based on the five previous years, fitted by time of year or time of year and time of day. For some variables, the preferred method forced the regression line through the origin.

Surprisingly, for many variables (T_a, RH, q, u, R_n, $SW_{\downarrow}$ and u), gaps of 3 months to 1 year were filled as well or almost as well as shorter gaps of 1 day to 1 month. The two exceptions were T_s and P. For most variables, the use of onsite rather than offsite related (x) time series, when available, reduced the mean absolute error by ~65% across all gap sizes.

Filling gaps

For each y time series with gaps to be infilled, an array of closely-related (similar) x time series from the same and nearby sites was first compiled, e.g. all air temperature measurements. The x time series were then ranked for goodness of fit based on the linear-regression ($y = a_0 + a_1x$) F statistic. Once ranked, the x time series were used sequentially to fill gaps in y until all gaps were filled. The infilling was done annually using a 14-month period from the previous Dec through the following Jan.

The BERMS network of sites is well suited to infilling approaches that require independent, related (x) time series, because of frequent measurement redundancy at the same site and the close proximity of the four sites. The outcome, in most cases, is high confidence in the infilled values. The most difficult gaps to fill are for precipitation in cases when the total accumulation across the gap is unknown.

Appendix C Long-term Continuity of the Flux Time Series

We assessed the long-term stability of the eddy-covariance measurements based on annual analyses of energy-balance closure, the computed u_*^{TH} filter, and the random uncertainty in NEE. In particular, we looked for discontinuities in the measured fluxes that may have been introduced by the changeover from the UBC closed-path to the LI-COR closed path eddy-covariance instrumentation and software at OBS in 2018 and OJP in 2012.

Annual consistency of energy-balance closure

The annual energy-closure fraction CF at the forest sites showed some evidence of decline over the study period. The blended CF mean (± s.d.) for the three forest sites was 0.84 ± 0.04, with small differences among sites (0.84 ± 0.05 (OA, 1997-2017), 0.82 ± 0.04 (OBS, 2000-2022), and 0.84 ± 0.03 (OJP, 2000-2022)) (Fig. C1, left panel). CF was slightly higher in the earlier than later years; between 1997-2010 and 2011-22, the mean CF dropped from 0.86 to 0.79 at OA, 0.84 to 0.81 at OBS, and 0.87 to 0.83 at OJP. The decline in CF may be related to instability in the EC measurement of $H + \lambda E$, perhaps related to a loss of low-frequency contributions to the flux as the sample tube became contaminated (Kidston et al., 2010). It may also be related to drift in the independent measurement of surface available energy $R_n - Q$.

The measurement of R_n was relatively stable over the study period, however, the Q / R_n ratio declined at all three sites (Fig. C1, right panel), related almost entirely to a declining Q_b /R_n ratio and accounting for 1-3% of the decline in CF. We believe the decline in Q_b to be anomalous, related to our failure to remeasure the depth of the tree bole temperature sensors as the trees grew in diameter, so that the mean tree bole temperature was not adequately sampled. At OJP, another possibility for the declining CF is changing instrumentation for net radiation: the shortwave and longwave radiometers used to calculate R_n were replaced with different instruments in 2011 and a different EC system was installed in 2012; these dates correspond to a step reduction in CF at OJP, from 0.87± 0.02 to 0.82 ± 0.02 (Fig. C1, left panel).

https://doi.org/10.5194/essd-2024-492
Preprint. Discussion started: 26 June 2025

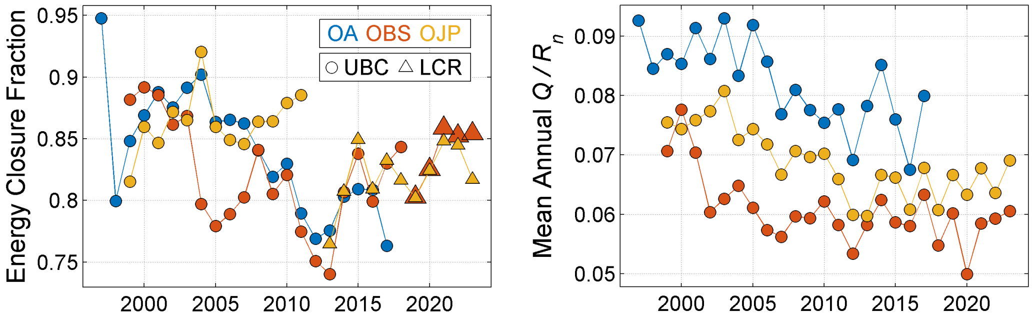

Figure C1 Left panel: Annual energy-balance closure fraction for the BERMS forest sites, based on daytime, warm-season periods. The change in symbol at OBS and OJP reflects the changeover from the UBC to the LI-COR (LCR) closed-path eddy-covariance system (Section 3.2.3). Right panel: Mean annual ratios of surface energy storage fluxes to net radiation for the BERMS forest sites, based on daytime, warm-season periods.

Stability and clarity of the u_*^{TH} filter

The clarity (Fig. C2) and stability (Fig. C3, upper panels) of the u_*-threshold filter u_*^{TH} as identified by change-point detection (Barr et al., 2013) also showed differences among sites and changes over time. At OA and OBS, the annual estimates of the u_*^{TH} were extremely well defined, with most of the 1,000 Monte-Carlo repetitions yielding a significant u_*^{TH} value ($p \leq 0.05$; Fig. C2, left panel), and nearly all showing the expected deficit mode (Fig. C2, right panel) (Barr et al., 2013). The deficit mode indicates that the magnitude of NEE decreases at low u_* values (below the u_*^{TH}), so that the use of a u_*^{TH} filter is warranted to resolve the problem of flux undermeasurement under low windspeed conditions at night. At OJP, the u_*^{TH} analysis showed a distinct "deficit" mode, but the change point was less well defined, with only 70% of the Monte-Carlo repetitions yielding a significant u_*^{TH} value, compared with 95% at OA and 98% at OBS. The definition of the change point at OBS and OJP was similar for the UBC and LI-COR closed-path EC systems. At the Fen, u_*^{TH} was poorly defined, with only 47% of the repetitions showing a "deficit" mode, meaning that the magnitude of NEE did not consistently decline at low values of u_*. Despite the poor u_*^{TH} definition at the Fen, an annual estimate of the u_*^{TH} was computed at all four sites as the median of the Monte-Carlo repetitions that yielded a significant u_*^{TH} in deficit mode.

https://doi.org/10.5194/essd-2024-492
Preprint. Discussion started: 26 June 2025

Open Access
Earth System Science Data
Discussions

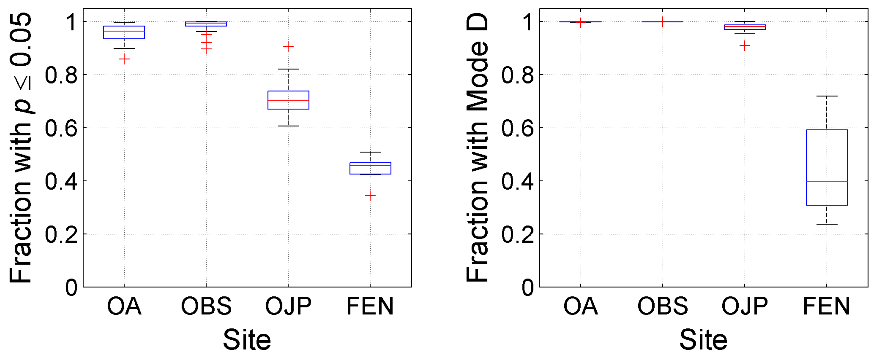

Figure C2 Evaluation of change-point detection in identifying a distinct value for the u_*^{TH} filter at the four BERMS sites. The left panel shows the fraction of 1,000 Monte-Carlo repetitions that yielded a significant u_*^{TH} change-point at the 5% level of significance. The right panel shows the fraction of the repetitions with an identifiable "D" or "deficit" mode, in which the magnitude of NEE decreased at low u_* values (below the u_*^{TH}).

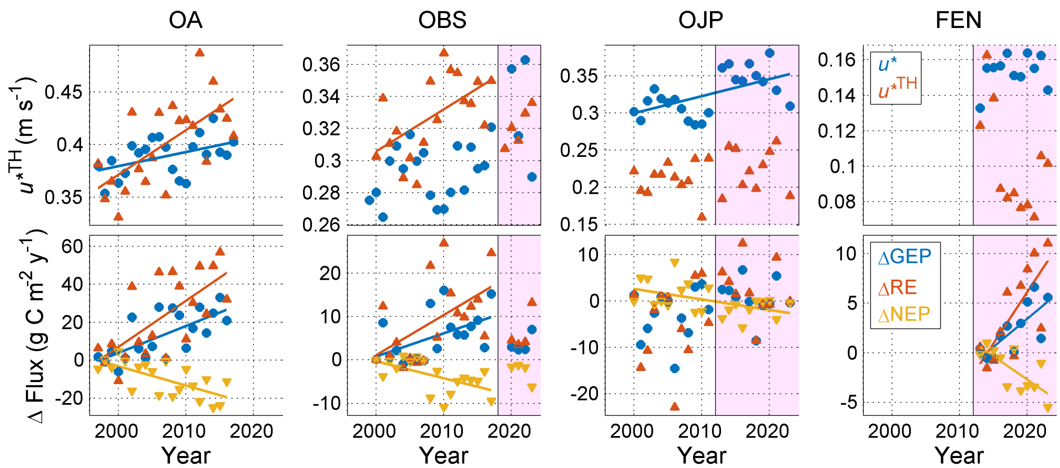

Figure C3 Upper panels: Mean annual values of the friction velocity u_* and median annual values of the u_*-threshold filter u_*^{TH} at the BERMS sites (upper panel). Lower panels: the impact of using an annual versus fixed estimate of u_*^{TH} on annual net ecosystem production (ΔNEP), ecosystem respiration (ΔR_e), and gross ecosystem production (ΔGEP). The Δ values are the difference of the estimates with an annual versus a fixed u_*^{TH}, where the fixed values are the original estimates of 0.35 m s^{-1} (OA), 0.30 m s^{-1} (OBS), 0.25 m s^{-1} (OJP), and 0.12 m s^{-1} (Fen) from earlier in the study. The white and shaded areas show the changeover in EC systems from the original UBC system (white) to the LI-COR closed-path system (shaded) (Section 3.2.3). Least-squares linear regression lines are shown when the regression is significant at the 5% level; the regression analysis at OBS only is limited to the years with the UBC EC system.

Analysis of long-term changes in the annual u_*^{TH} showed differences among sites (Fig. C3, upper panels). At OA, where all years used the UBC EC system, u_*^{TH} had a significant positive trend, increasing by ~20% between 1997 and 2017, from 0.36 to 0.44 m s^{-1}. At OBS, u_*^{TH} increased by ~15% over the years with the UBC EC system (1999-2018), followed by a step down in 2019-2022 (years with the LI-COR closed-path EC system). At OJP and Fen, no significant

https://doi.org/10.5194/essd-2024-492
Preprint. Discussion started: 26 June 2025

Open Access Earth System Science Data Discussions

changes in the annual u_*^{TH} were found. One plausible cause of the increasing u_*^{TH} at OA and OBS is an increase in aerodynamic roughness as the stands aged, although a similar response would be expected at OJP. High tree mortality at OA and OJP may have increased canopy roughness, with a decline in stand density from 980 stems ha^{-1} in 1994 to 473 stems ha^{-1} in 2016 at OA, and 1317 stems ha^{-1} in 1994 to 645 stems ha^{-1} in 2023 at OJP. Note also that the increase in u_*^{TH} at OA is associated with an increase in u_* (Fig. C3, upper-left panel).

Our practice to date has been to use fixed, site-specific values for the u_*^{TH} of 0.35 m s^{-1} (OA), 0.30 m s^{-1} (OBS), 0.25 m s^{-1} (OJP), and 0.12 m s^{-1} (Fen), based on our earlier analysis. To evaluate the impact of the observed increases in the annual u_*^{TH}, we recalculated the annual C fluxes of using annual rather than fixed u_*^{TH} values. Relative to the fixed u_*^{TH} values above, the use of annual u_*^{TH} values altered mean annual NEP = GEP - R_e from 127 = 1051 - 924 g C m^{-2} y^{-1} to 117 = 1064 - 947 g C m^{-2} y^{-1} at OA and from 52 = 808 - 756 g C m^{-2} y^{-1} to 48 = 813 - 765 g C m^{-2} y^{-1} at OBS, with little effect on the annual means at OJP and Fen. Fig. C3 (lower panel) shows the impact on an annual basis, where ΔNEP, ΔRE, and ΔGEP are the differences between the annual C flux estimates with a fixed u_*^{TH} value and those with varying, annual u_*^{TH} estimates. The differences show significant temporal trends that reflect the observed increases in the u_*^{TH}. These impacts, although subtle, are large enough to warrant the use of annual u_*^{TH} estimates at these sites. This has not been done.

Random uncertainty

Random uncertainty in annual NEP, GEP and R_e estimated using the Richardson-Hollinger method (Section 3.2.9) varied among sites but was mostly stable over the period of measurement at each site (Fig. C4). The random uncertainty in annual GEP averaged 6%, 6%, 9% and 9% of annual mean GEP at OA, OBS, OJP, and Fen, respectively, compared to 8%, 9%, 12% and 14% of mean annual R_e. The random uncertainty in NEP, although smaller than that of GEP and R_e, was large when compared to mean annual NEP, with mean values of 42 versus 128 g C m^{-2} y^{-1}, respectively, at OA, 33 versus 51 g C m^{-2} y^{-1} at OBS, 36 versus 30 g C m^{-2} y^{-1} at OJP, and 22 versus 22 g C m^{-2} y^{-1} at Fen. In general, the random uncertainty in annual NEP was most affected by the length of the largest data gap; the extreme uncertainty value at OA in 2011 is associated with a 39-day gap during July and Aug of that year. The random uncertainty in annual NEP showed no clear temporal trends except at OBS and OJP where its mean value increased following the changeover of the EC system, from 32 ± 4 g C m^{-2} s^{-1} (2000-2017, with a gradual increase after 2009) to 39 ± 2 g C m^{-2} s^{-1} at OBS (2020-2023), and from 33 ± 5 g C m^{-2} s^{-1} (2000-2011) to 41 ± 6 g C m^{-2} s^{-1} at OJP (2013-2023) (Fig. C4).

https://doi.org/10.5194/essd-2024-492
Preprint. Discussion started: 26 June 2025

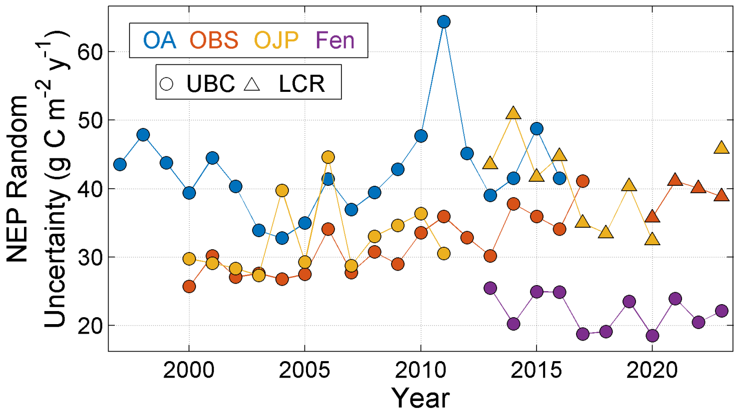

Figure C4 Random uncertainty in annual NEP. The change in symbol at OBS and OJP reflects the change in eddy-covariance system (Section 3.2.3). Years were excluded from the analysis with data gaps of two months or longer.

The increase in NEP random uncertainty following the EC-system changeover reflects higher levels of NEE random noise for the LI-COR closed-path EC system than the UBC EC system (Fig. C5). At OBS, an ~30% difference between the two EC systems spanned at all magnitudes of NEE, including both negative (warm-season, daytime) and positive (cold-season and nighttime) NEE values. At OJP, a similar 30% difference was found for negative NEE only; for reasons we do not understand, the two EC systems at OJP produced similar noise characteristics for positive NEE. It is difficult to assess whether the EC system changeovers at OBS and OJP introduced discontinuities into the flux time series, and our evaluations are inconclusive. While a distinct difference is evident in the noise characteristics of the two EC systems, we see no indications that the higher levels of random noise and uncertainty from the LI-COR closed-path EC system also introduced a discontinuity or bias in the NEE time series.

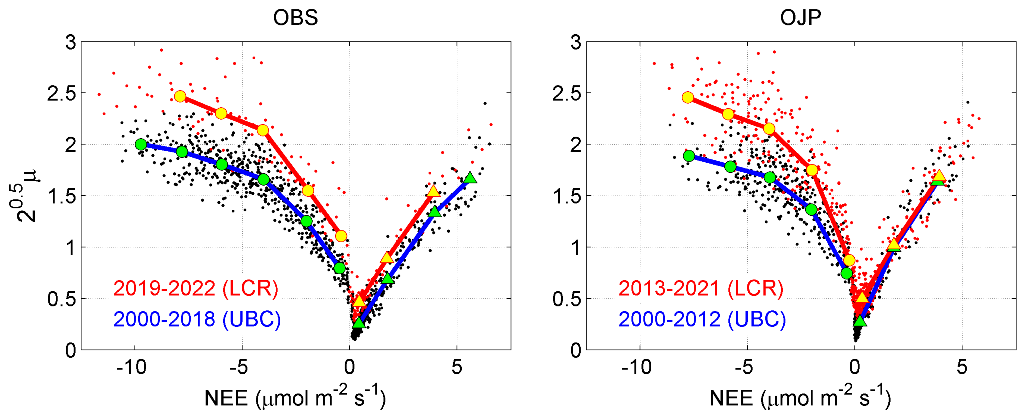

Figure C5 Random noise characteristics of the two eddy-covariance systems that were deployed at the BERMS OBS and OJP flux towers (LCR: LI-COR closed path EC instrumentation and software; UBC: UBC BIOMET instrumentation and software). The y axis shows a fitted coefficient from a double-exponential distribution, in relation to NEE, with separate

https://doi.org/10.5194/essd-2024-492
Preprint. Discussion started: 26 June 2025

analyses for positive and negative NEE values; see Richardson et al. (2006) for further details. The solid lines and symbols
925 **show binned means of individual points from the annual analyses.**

Cold-Season NEE shift

The strongest indication that the EC-system changeover at OBS and OJP affected the continuity of the NEE time series is a shift in cold-season NEE following the changeover. The step-change, as shown in Fig. C6 for extended
930 daytime and nighttime periods, is striking, especially during the day, and may indicate bias between the systems. Many of the half-hourly daytime LI-COR closed-path NEE values (not shown) are near or below zero, especially at OJP, which is implausible during the cold season.

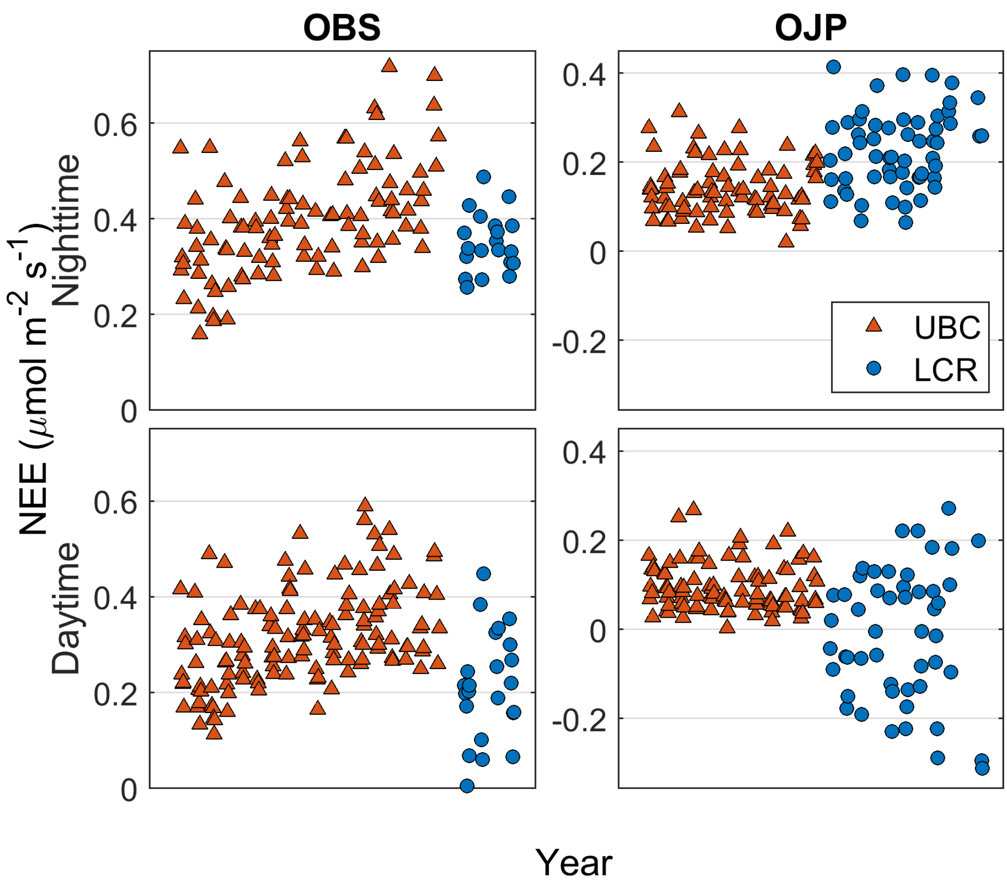

935 **Figure C6. Effect of the changeover in EC systems at OBS and OJP on cold-season net ecosystem exchange NEE. Caption: UBC - UBC BIOMET instrumentation and software; LIC - LI-COR closed-path EC system with EddyPro software. Each point is the mean of 240 (or more) data points. For each year (treating each Oct to April period separately), cold-season periods were selected when air temperature was below 0.0 ºC and soil temperature was below -0.1 ºC; the selected periods**

https://doi.org/10.5194/essd-2024-492
Preprint. Discussion started: 26 June 2025

were stratified as daytime or nighttime; and NEE was averaged for periods of between 240 and 358 non-missing data points, depending on the total number of data points.

Figure C7 compares the median daily cycles of cold-season NEE from before and after the EC-system changeovers at OBS and OJP (averaged for Jan and Feb, all measurement years). The inserts show the median NEE values for each half-hour in the daily cycle in relation to the median sensible heat flux *H*. Cold-season NEE at these sites results from R_e alone and should therefore be relatively constant throughout the day in winter. Two features from Fig. C7 are striking: the difference between the UBC and LI-COR systems, with relatively constant NEE throughout the day from the UBC system but a marked daytime decline in NEE from the LI-COR system; and the strong relationship between half-hourly median NEE from the LI-COR system and the sensible heat flux *H*, contrasted with the relatively flat NEE versus *H* response of the UBC system over the daily cycle (Fig. C7, inserts). (Although the Fen also uses the LI-COR closed path EC system, its daily NEE cycle is flat, presumably because the site's open snow cover and high albedo result in nearly constant *H* over the daily cycle.) The association of the negative daytime anomaly in NEE and the daytime rise in *H* at OBS and OJP suggests a possible issue with the LI-7200 sample cell temperature measurement used in the calculation of the CO_2 mixing ratio and CO_2 flux, however we have not been able to isolate or resolve the specific cause.

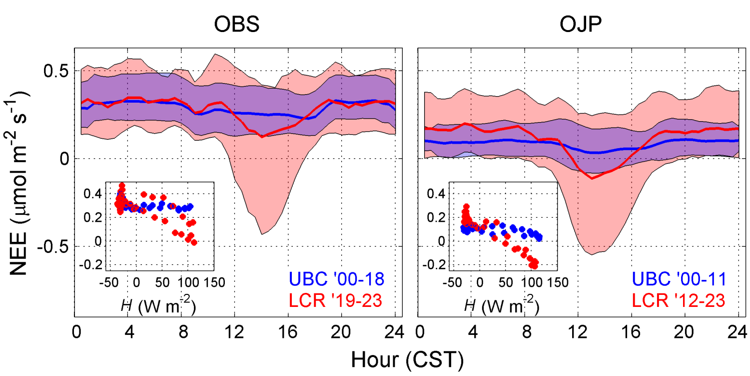

Figure C7. Mean daily NEE cycle for Jan and Feb, comparing the two closed-path eddy-covariance systems at OBS and OJP. The solid lines show the median daily cycle; the shaded areas show the interquartile range (25th to 75th percentiles). Daytime is ~0930 to ~1700. The insert in the lower-left corner shows the half-hourly NEE medians from the main figure in relation to the half-hourly median sensible heat flux *H*. Caption: UBC - UBC BIOMET instrumentation and software; LCR - LI-COR closed-path EC system with EddyPro software.

The net effect of the EC-system changeover on cumulative winter NEP (summed from Dec 21 to Mar 21 each year) is shown in Fig. C8, in relation to mean soil temperature. Note the negative correlation at both sites (correlation coefficient -0.51 OBS, -0.36 OJP, using all data), indicating increasing winter C losses at warmer soil temperatures. Note also the rather subtle differences between the UBC and LI-COR closed-path EC systems. At OBS, the four years with the LI-COR system have slightly elevated winter NEP compared to the UBC system, but the mean shift is small, ~ 5 g C m^{-2} over the 3-month period. At OJP, the NEE-*Ts* relationship appears to be quite similar between the two

https://doi.org/10.5194/essd-2024-492
Preprint. Discussion started: 26 June 2025

EC systems, despite the pronounced EC-system effects on NEE in Figs. C6 and C7. Apparently, the opposite daytime and nighttime NEE responses to the EC-system changeover at OJP (Fig. C6) partially offset each other and minimize the bias in the winter totals. We conclude that the EC-system changeovers affected the continuity of the NEE time series at OBS and OJP, but that the impact was not so large as to invalidate analyses that encompass the complete time series, such as long-term changes in the C cycle or climatic controls on seasonal and interannual variability.

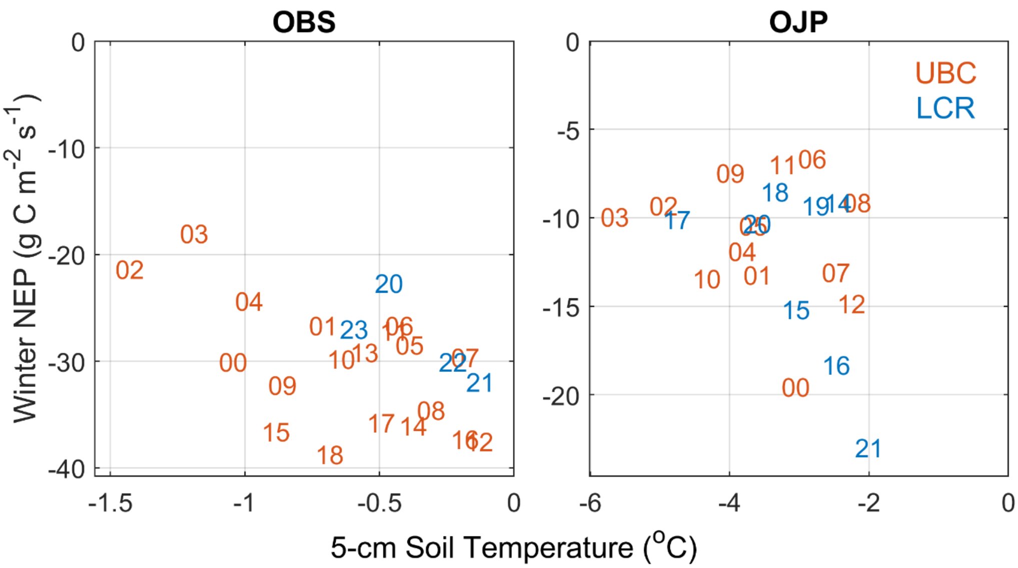

Figure C8. Effect of the changeover in EC systems at OBS and OJP on the relationship between winter (Dec 21 to Mar 21) cumulative net ecosystem exchange NEE and mean 5-cm soil temperature. Caption: UBC - UBC BIOMET instrumentation and software; LCR - LI-COR closed-path EC system with EddyPro software.

https://doi.org/10.5194/essd-2024-492
Preprint. Discussion started: 26 June 2025

Appendix D Known Issues in Meteorological Data

Long-term drift in PPFD

We evaluated long-term drift in the incoming PPFD ($PPFD_{\downarrow}$) measurement by comparing $PPFD_{\downarrow}$ with incoming shortwave radiation $SW_{\downarrow}$, which in turn was evaluated in relation to the computed top-of atmosphere shortwave radiation $SW_{\downarrow}^{TOA}$. Based on the long-term stability of the annual ratio $SW_{\downarrow}$ / $SW_{\downarrow}^{TOA}$ (the atmospheric shortwave transmittance, Fig. D1, left panel), we concluded that the measurement of $SW_{\downarrow}$ was stable. (The first two measurement years (2002-2003) at Fen are an anomaly due to poor sensor calibration.) In contrast, the annual ratio of $PPFD_{\downarrow}$/ $SW_{\downarrow}$ ((μmol m^{-2} s^{-1}) / (W m^{-2})) declined after 2010 (Fig. D1, right panel). At the three forest sites, annual mean $PPFD_{\downarrow}$ / $SW_{\downarrow}$ remained relatively stable between 1997 and 2010, with annual means of 1.98 ± 0.02 (μmol m^{-2} s^{-1}) / (W m^{-2}) at OA, 2.01 ± 0.02 at OBS, and 1.99 ± 0.01 at OJP. After 2010, however, the $PPFD_{\downarrow}$ / $SW_{\downarrow}$ ratio began to decline, with a mean annual decline of -0.022 ((μmol m^{-2} s^{-1}) / (W m^{-2})) y^{-1} at OA, -0.027 at OBS and -0.032 at OJP. By 2019-2021, the mean $PPFD_{\downarrow}$ / $SW_{\downarrow}$ ratios of 1.70 (μmol m^{-2} s^{-1}) / (W m^{-2}) at OBS and 1.66 at OJP were 16% lower than the 1998-2010 means. The decline was even more serious at the Fen. (The anomaly at the Fen in 2002-2003 is related to the aberrantly low $SW_{\downarrow}$ in these years.)

The similarities in the rate of the $PPFD_{\downarrow}$ / $SW_{\downarrow}$ decline among the forest sites are noteworthy. The most likely cause is PPFD sensor degradation over time. At the three forest sites (but not the Fen), new PPFD sensors were deployed approximately every five years up to and including 2007, but no new sensors were deployed after 2007. At the Fen, the PPFD sensors were not new when installed and were never replaced. Based on the observed decline in $PPFD_{\downarrow}$ / $SW_{\downarrow}$, the PPFD values after 2010 were adjusted to preserve an expected $PPFD_{\downarrow}$ / $SW_{\downarrow}$ mean of 1.99 (μmol m^{-2} s^{-1}) / (W m^{-2}). A similar decline in PPFD quantum sensor response has been reported elsewhere, related to a decline in the blue-light sensitivity of the photodiode (Korde and Geist, 1987). In all likelihood, a similar drift after 2010 occurred in the measurement of outgoing and understory PPFD, however, we have no way to evaluate its magnitude, and so no correction was applied.

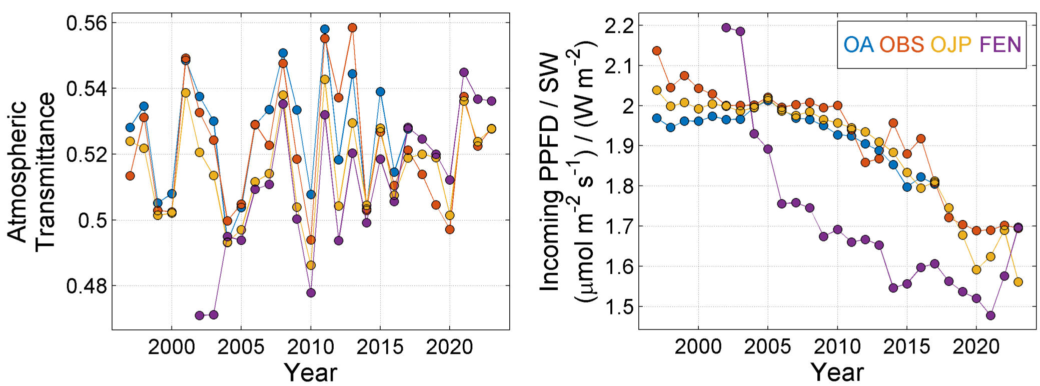

Figure D1 Mean annual values of atmospheric shortwave transmittance ($SW_{\downarrow}$ / $SW_{\downarrow}^{TOA}$, left panel); and the ratio of

https://doi.org/10.5194/essd-2024-492
Preprint. Discussion started: 26 June 2025

incoming PPFD to incoming shortwave radiation ($PPFD_{\downarrow}$/ $SW_{\downarrow}$, right panel, units (μmol m^{-2} s^{-1}) / (W m^{-2})), at the four BERMS sites, 1997-2023. Both metrics are based on daytime periods with $SW_{\downarrow}^{TOA}$ above 50 W m^{-2}.

D2 Discontinuities in soil VWC

The soil VWC measurement had a number of unresolvable issues which resulted in discontinuities in the soil VWC time series. At OA, a discontinuity occurred at all depths in 2007-2008, related to the installation of a second TDR transect with different instrumentation (CSI TDR100) in late summer 2007 followed by the discontinuation of the original (ESI MoisturePoint) system in late 2008. The original system and transect included probes in a small depressional clearing that flooded in 2004 and remained flooded afterwards, as seen in the high VWC values from 2004-2007 (Fig. D2). The replacement system was installed in late summer 2007 at a slightly higher elevation in an area that was free from flooding and more typical of the flux footprint. Note that the change of TDR transect and system affected all depths, making it difficult to compare the data before and after 2007. For instance, an anomaly associated with the discontinuity in soil VWC is evident at the 0-15 cm depth (Fig. D2), where the data incorrectly indicate greater summer soil-water drawdown in 2009-2014 than during the 2001-2003 drought. Independent measurements using CSI CS615 probes at 2.5 and 7.5 cm depth indicate a similar summer VWC minima for 2001-2003 and 2009-2014.

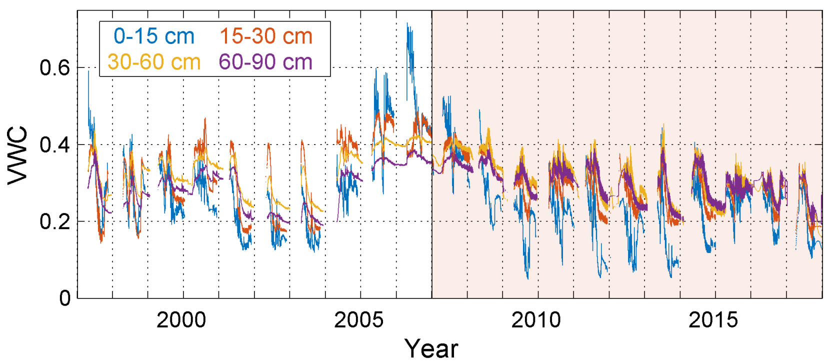

Figure D2 Measured soil VWC at the BERMS Old Aspen site, for periods when the soil was not frozen. The shaded area after 2007 indicates a change in the TDR instrumentation, from the original ESI MoisturePoint system in a depressional forest clearing to the CSI TDR 100 system at slightly higher elevation.

At OJP, which had two soil VWC profiles at six depths each, four of the twelve soil-water-content sensors had one or more abrupt and unexplained discontinuities. The data were rejected after the discontinuities, however, the sensors have not been replaced. To maintain a robust mean VWC time series at each depth, the missing data after the discontinuity were filled based on long-term relationships with the most similar complete time series, from the same site and depth where possible. Filling the long gaps, although imperfect, circumvented the issue of otherwise serious discontinuities in the mean time series at each depth.

At OBS, which had two soil VWC profiles at five depths each, six of ten sensors either failed during the measurement period or had serious, unresolved discontinuities. The issues were most serious at the 2.5-, 45- and 60-90-cm depths, and remain unresolved. Because of this, only the 7.5- and 22.5-cm depths have been included in the archive.

Author contributions

Andy Black and Zoran Nesic were responsible for the eddy-covariance flux measurements using the UBC closed-path system at OA (1997-2017) and OBS (1999-2018). They also provided expert advice for the flux measurements at OJP and Fen. Harry McCaughey (now deceased) was responsible for the eddy-covariance flux measurements using the UBC closed-path system at OJP (1999-2012); Newell Hedstrom was responsible for the eddy-covariance flux measurements using the LI-COR open-path system at Fen (2002-2010); and Warren Helgason and Bruce Johnson were responsible for the eddy-covariance flux measurements using the LI-COR closed-path system at OBS (2019-2023), OJP (2013-2023), and Fen (2013-2023). Alan Barr oversaw the meteorological and soil measurements at all sites for 1997-2012, followed by Warren Helgason and Bruce Johnson (2013-2023). Alan Barr, Charmaine Hrynkiw, Amber Ross, and Bruce Johnson managed the data. Alan Barr drafted the paper, with guidance, comments and revisions from Andy Black, Warren Helgason, and Andrew Ireson, and help from Bruce Johnson in developing Appendix A.

Competing interests

The authors declare that they have no conflict of interest.

Acknowledgements

The authors wish to thank the many government and funding agencies that have provided financial support over 1997-2024: Environment Canada (now Environment and Climate Change Canada), the Canadian Forest Service), Parks Canada, the Natural Sciences and Engineering Research Council of Canada, the Canadian Foundation for Climate and Atmospheric Science, and BioCap Canada, as well as the research networks and institutes they supported: the Fluxnet-Canada Research Network (FCRN), the Canadian Carbon Program (CCP), the Global Institute for Water Security (GIWS), the Changing Cold Regions Network, Global Water Futures, and the Global Water Futures Observatories. Prior to the inception of BERMS, the vision and leadership of Piers Sellers and Forrest Hall (NASA) in BOREAS created an exemplary model for BERMS to follow, with strengths in multidisciplinary science, measurement standardization, the integration of field measurement programs with process understanding and modelling, and a strong commitment to data management. Barry Goodison (ECCC), Bob Stewart (CFS), and Norm Stolle (Parks) championed the BERMS program through its early years, followed by strong support from Hank Margolis (FCRN, CCP), Anne Walker (ECCC), and Howard Wheater (GIWS). Many have contributed to field support over the years, including Rick Ketler, Andrew Suyker, Greg Neufeld, Dan Matthews, Bruce Cole, Joe Eley, Craig Smith, Erin

Thompson, Dell Bayne, and Cody David. Data-management support was provided by Erin Thompson, Steve Enns, Nick Grant, and Paul Jassal.

References

Amiro, B. D., Barr, A. G., Black, T. A., Iwashita, H., Kljun, N., McCaughey, J. H., Morgenstern, K., Murayama, S., Nesic, Z., Orchansky, A. L., and Saigusa, N.: Carbon, energy and water fluxes at mature and disturbed forest sites, Saskatchewan, Canada, Agric. For. Meteorol., 136, 237-251. https://doi.org/10.1016/j.agrformet.2004.11.012, 2006.

Anderson, D.W.: BOREAS TE-01 SSA Soil Lab Data. Data set. Available on-line [http://www.daac.ornl.gov] from Oak Ridge National Laboratory Distributed Active Archive Center, Oak Ridge, Tennessee, U.S.A. https://doi.org/10.3334/ORNLDAAC/530, 2000.

Baldocchi, D. D., Vogel, C. A., and Hall, B.: Seasonal variation of carbon dioxide exchange rates above and below a boreal jack pine forest, Agric. For. Meteorol., 83, 147–170. https://doi.org/10.1016/S0168-1923(96)02335-0, 1997.

Barr A. G., Black, T. A., Hogg, E. H., Kljun, N., Morgenstern, K., and Nesic, Z.: Inter-annual variability in the leaf area index of a boreal aspen-hazelnut forest in relation to net ecosystem production, Agric. For. Meteorol. 126, 237-255, https://doi.org/10.1016/j.agrformet.2004.06.011, 2004.

Barr, A. G., Black, T. A., Hogg, E. H., Griffis, T. J., Morgenstern, K., Kljun, N., Theede, A., and Nesic, Z.: Climatic controls on the carbon and water balances of a boreal aspen forest, 1994–2003, Global Change Biology, 13(3), 561-576. https://doi.org/10.1111/j.1365-2486.2006.01220.x, 2007.

Barr, A. G., van der Kamp, G., Black, T. A., McCaughey, J. H., and Nesic, Z.: Energy balance closure at the BERMS flux towers in relation to the water balance of the White Gull Creek watershed 1999–2009, Agric. For. Meteorol., 153, 3-13, https://doi.org/10.1016/j.agrformet.2011.05.017, 2012.

Barr A. G., Richardson A. D., Hollinger D. Y., Papale D., Arain M. A., Black T. A., Bohrer G., Dragoni D., Fischer M. L., Gu L., Law B. E., Margolis H. A., McCaughey J. H., Munger J. W., Oechel W., Schaeffer K..: Use of change-point detection for friction-velocity threshold evaluation in eddy-covariance studies, Agric. Forest Meteorol., 171–172, 31–45, https://doi.org/10.1016/j.agrformet.2012.11.023, 2013.

Black, T. A., Den Hartog, G., Neumann, H. H., Blanken, P .D., Yang, P. C., Russell, C., Nesic, Z., Lee, X., Chen, S. G., Staebler, R., and Novak, M. D.: Annual cycles of water vapour and carbon dioxide fluxes in and above a boreal aspen forest, Global Change Biology, 2, 219-229, https://doi.org/10.1111/j.1365-2486.1996.tb00074.x,1996.

Blanken, P. D., Black, T. A., Yang, P. C., Neumann, H. H., Nesic, Z., Staebler, R., den Hartog, G., Novak, M. D., and Lee, X.: Energy balance and canopy conductance of a boreal aspen forest: Partitioning overstory and understory components, J. Geophys. Res., 102, 28915-28927, https://doi.org/10.1029/97JD00193, 1997.

Chen J. M., Govind, A., Sonnentag, O., Zhang, Y., Barr, A., and Amiro, B.: Leaf area index measurements at Fluxnet Canada sites, Agric. Forest Meteorol., 140, 257-268., https://doi.org/10.1016/j.agrformet.2006.08.005, 2006.

ESTR Secretariat: Boreal Plains Ecozone: evidence for key findings summary. Canadian Biodiversity: Ecosystem Status and Trends 2010, Evidence for Key Findings Summary Report No. 12. Canadian Councils of Resource Ministers. Ottawa, ON. https://biodivcanada .chm-cbd.net/ecosystem-status-trends-2010/boreal-plains-summary, 2014.

Flatau, P. J., Walko, R. L., and Cotton, W. R.: Polynomial fits to saturation vapor pressure, J. Appl. Met., 31, 1507-1513, https://www.jstor.org/stable/26186606, 1992.

Foken, T., Gockede, M., Mauder, M., Mahrt, L., Amiro, B. D., and Munger, J. W.: Edited by X. Lee, et al. Post-field quality control, in Handbook of Micrometeorology: A Guide for Surface Flux Measurements, Dordrecht: Kluwer Academic, 81-108, 2004.

Gaumont-Guay, D., Black, T. A., Barr, A. G., Griffis, T. J., Jassal, R. S., Krishnan, P., Grant, N., and Nesic, Z.: Eight years of forest-floor CO2 exchange in a boreal black spruce forest: spatial integration and multi-temporal trends, Agric. Forest Meteorol., 184, 25-35, https://doi.org/10.1016/j.agrformet.2013.08.010, 2014.

Goulden, M. L., Munger, J. W., Fan, S., Daube, B. C. and Wofsy, S. C.: Measurements of carbon sequestration by long-term eddy covariance: Methods and a critical evaluation of accuracy, Global Change Biology, 2(3), 169-182. https://doi.org/10.1111/j.1365-2486.1996.tb00070.x, 1996.

Gower, S. T., Vogel, J. G., Norman, J. M., Kucharik, C. J., Steele, S. J., and Stow, T.K.: Carbon distribution and aboveground net primary production in aspen, jack pine, and black spruce stands in Saskatchewan and Manitoba, Canada, J. Geophys. Res., 102(D24), 29029-29041, https://doi.org/10.1029/97JD02317, 1997.

Griffis, T. J., Black, T. A., Morgenstern, K., Barr, A. G., Nesic, Z., Drewitt, G. B., Gaumont-Guay, D., and McCaughey, J. H.: Ecophysiological controls on the carbon balances of three southern boreal forests, Agric. For. Meteorol.,117, 53-71, https://doi.org/10.1016/S0168-1923(03)00023-6, 2003.

Griffis, T. J., Black, T. A., Gaumont-Guay, D., Drewitt, G. B., Nesic, Z., Barr, A. G., Morgenstern, K. and Kljun, N.: Seasonal variation and partitioning of ecosystem respiration in a southern boreal aspen forest, Agric. For. Meteorol., 125, 207-223, https://doi.org/10.1016/j.agrformet.2004.04.006, 2004.

Harder, P. and Pomeroy, J.: Estimating precipitation phase using a psychrometric energy balance method, Hydrological Processes, 27, 1901–1914, https://doi.org/10.1002/hyp.9799, 2013.

Helbig, M., Waddington, J. M., Alekseychik, P., Amiro., B. D., Aurela, M., Barr, A. G., Black, T. A., Blanken, P. D., Carey, S. K., Chen, J., Chi, J., Desai, A. R., Dunn, A., Euskirchen, E. S., Flanagan, L. B., Forbrich, I., Friborg, T., Grelle, A., Harder, S., Heliasz, M., Humphreys, E. R., Ikawa, H., Isabelle, P-E., Iwata, H., Jassal, R., Korkiakoski, M., Kurbatova, J., Kutzbach, L., Lindroth, A., Lofvenius, M. O., Lohila, A., Mammarella, I., Marsh, P., Maximov, T., Melton, J. R., Moore, P. A., Nadeau, D. F., Nicholls, E. M., Nilsson, M. B., Ohta, T., Peichl, M., Petrone, R. M., Petrov, R., Prokushkin, A., Quinton, W. L., Reed, D. E., Roulet, N. T., Runkle, B. R. K., Sonnentag, O., Strachan, I. B., Taillardat, P., Tuittila, E-S., Tuovinen, J-P., Turner, J., Ueyama, M., Varlagin, A., Wilmking, M., Wofsy, S. C., and Zyrianov, V.: Increasing contribution of peatlands to boreal

https://doi.org/10.5194/essd-2024-492
Preprint. Discussion started: 26 June 2025

evapotranspiration in a warming climate, Nature Climate Change, 10, 2020, 555–560, https://doi.org/10.1038/s41558-020-0763-7, 2020.

Helgason, W., Johnson, B., David, C., Barr, A. and Black A.: Long-term meteorological and carbon, water, and energy flux data from the Boreal Ecosystem Research and Monitoring Sites, Saskatchewan, Canada. Federated Research Data Repository, https://doi.org/10.20383/103.01063, 2024.

Hogg, E.H.: Temporal scaling of moisture and the forest-grassland boundary in western Canada. Agric. For. Meteorol., 84, 115-122, https://doi.org/10.1016/S0168-1923(96)02380-5, 1997.

Hyland, R.W., and Wexler, A.: Formulations for the thermodynamic properties of the saturated phases of H_2O from 173.15 K to 473.15 K, ASHRAE Transactions, 89(2A), 500-519, 1983.

Ireson A. M., Barr, A. G., Johnstone, J. F., Mamet, S. D., van der Kamp, G., Whitfield, C. J., Michel, N. L., North, R. L., Westbrook, C. J., DeBeer, C., Chun, K. P., Nazemi, A., and Sagin, J.: The changing water cycle: the Boreal Plains ecozone of Western Canada, Wiley Interdisciplinary Reviews: Water, 2, 505–521, https://doi.org/10.1002/wat2.1098, 2015.

Iqbal, M.: An Introduction to Solar Radiation. Academic Press. Don Mills, Ontario, 389 pp., ISBN 0-12-373750-8, 1983.

Jarvis, P. G., Massheder, J. M., Hale, S. E., Moncrieff, J. B., Rayment, M., and Scott, S. L.: Seasonal variation of carbon dioxide, water vapor, and energy exchanges of a boreal black spruce forest, J. Geophys. Res., 102(D24), 28953-28966, http://doi.org/10.1029/97JD01176, 1997.

Keenan, T.F., Baker, I., Barr, A., Ciais, P., Davis, K., Dietze, M., Dragoni, D., Gough, C. M., Grant, R., Hollinger, D., Hufkens, K., Poulter, B., McCaughey, H., Rackza, B., Ryu, Y., Schaefer, K., Tian, H., Verbeeck, H., Zhao, M., and Richardson, A. D.: Evaluation of terrestrial biosphere models for land-atmosphere CO_2 exchange on inter-annual time scales: Results from the North American Carbon Program, Global Change Biology, doi: 10.1111/j.1365-2486.2012.02678.x, 2012.

Kidston J., Brümmer C., Black T. A., Morgenstern K., Nesic Z., McCaughey J. H., and Barr A. G.: Energy balance closure using eddy covariance over two different land surfaces and implications for CO_2 flux measurements, Bound. Layer Meteorol., 36, 193-218, https://doi.org/10.1007/s10546-010-9507-y, 2010.

Kljun, N., Black, T. A., Griffis, T. J., Barr, A. G., Gaumont-Guay, D., Morgenstern, K., McCaughey, J. H., and Nesic, Z.: Response of net ecosystem productivity of three boreal forest stands to drought, Ecosystems, 9, 1128-1144. https://doi.org/10.1007/s10021-005-0082, 2006.

Korde, R., and Geist, J.: Quantum efficiency stability of silicon photodiodes, Appl. Opt., 26, 5284-5290, https://opg.optica.org/ao/abstract.cfm?URI=ao-26-24-5284, 1987.

Krishnan, P., Black, T. A., Barr, A. G., Gaumont-Guay, D., Grant, N., and Nesic, Z.: Factors controlling the interannual variability in the carbon balance of a southern boreal black spruce forest. J. Geophys. Res. 113, D09109, doi:10.1029/2007JD008965, 2008.

https://doi.org/10.5194/essd-2024-492
Preprint. Discussion started: 26 June 2025

Krishnan, P., Black, T. A., Grant, N. J., Barr, A. G., Hogg, E. H., Jassal, R. S., and Morgenstern, K.: Impact of changing soil moisture distribution on net ecosystem productivity of a boreal aspen forest during and following drought, Agric. For. Meteorol., 139(3–4), 208-223, https://doi.org/10.1016/j.agrformet.2006.07.002, 2006.

Lambert, A., Huang, J., van der Kamp, G., Henton, S., Mazzotti, S., James, T. S., Courtier, N., and Barr, A. G.: A Positive Water Storage Anomaly in the Nelson River Basin from Gravity and GPS Observations: Quantitative Confirmation by Hydrological Measurements. Geophys. Res. Letters, 40, 6,118-6,122, 2013.

Liu, P., Barr, A. G., Zha, T., Black, T. A., Jassal, R. S., Nesic, Z., Helgason, W. D., Jia, X., and Tian, Y.: Re-assessment of the climatic controls on the carbon and water fluxes of a boreal aspen forest over 1996–2016: Changing sensitivity to long-term climatic conditions, Global Change Biology, 28 (15), pp. 4605-4619, doi: 10.1111/gcb.16218, 2022.

Liu, P., Black, T. A., Jassal, R. S., Zha, T., Nesic, Z., Barr, A. G., Helgason, W. D., Xia, J., Tian, Y., Stephens, J. J., and Ma, J.: Divergent long-term trends and interannual variation in ecosystem resource use efficiencies of a southern boreal old black spruce forest 1999–2017, Global Change Biology, 25, 3056-3069, https://doi.org/10.1111/gcb.14674, 2019.

McCaughey, J. H., and Saxton, W. L.: Energy balance terms in a mixed forest, Agric. For. Meteorol., 44, 1-18, https://doi.org/10.1016/0168-1923(88)90029-9, 1988.

Moffat, A. M., Papale, D., Reichstein, M., Hollinger, D. Y., Richardson, A. D., Barr, A. G., Beckstein, C., Braswell, B. H., Churkina, G., Desai, A. R., Falge, E., Gove, J. H., Heimann, M., Hui, D., Jarvis, A. J., Kattge, J., Noormets, A., and Stauch, V. J.: Comprehensive comparison of gap-filling techniques for eddy covariance net carbon fluxes, Agr. Forest Meteorol., 147, 209–232, https://doi.org/10.1016/j.agrformet.2007.08.011, 2007.

Papale, D., Reichstein, M., Aubinet, M., Canfora, E., Bernhofer, C., Kutsch, W., Longdoz, B., Rambal, S., Valentini, R., and Vesala, T.: Towards a standardized processing of Net Ecosystem Exchange measured with eddy covariance technique: algorithms and uncertainty estimation, Biogeosciences 3(4), 571-583. https://doi.org/10.5194/bg-3-571-2006, 2006.

Pulliainen, J., Aurela, M., Laurila, T., Aalto, T., Takala, M., Salminen, M., Kulmala, M., Barr, A., Heimann, M., Lindroth, A., Laaksonen, A., Derksen, C., Mäkelä, A., Markkanen, T., Lemmetyinen, J., Susiluoto, J., Dengel, S., Mammarella, I., Tuovinen, J.-P., and Vesala, T.: Early snowmelt significantly enhances boreal springtime carbon uptake, PNAS, 114(42), 11,081–11,086, 2017.

Reichstein, M., Falge, E., Baldocchi, D. D., Papale, D., Aubinet, M., Berbigier, P., Bernhofer, C. ... Valentini, R.: On the separation of net ecosystem exchange into assimilation and ecosystem respiration: review and improved algorithm, Global Change Biology, *11*(9), 1424-1439, https://doi.org/10.1111/j.1365-2486.2005.001002.x, 2005.

Richardson, A. D., Anderson, R. S., Arain, M. A., Barr, A. G., Bohrer, G., Chen, G., Chen, J. M., Ciais, P., Davis, K. J., Desai, A. R., Dietze, M. C., Dragoni, D., Garrity, S. R., Gough, C. M., Grant, R., Hollinger, D. Y., Margolis, H. A., McCaughey, H., Migliavacca, M., … Xue, Y.; Terrestrial biosphere models need better representation of

https://doi.org/10.5194/essd-2024-492
Preprint. Discussion started: 26 June 2025

vegetation phenology: Results from the North American Carbon Program Site Synthesis, Global Change Biology, 18(2), 566–584, 10.1111/j.1365-2486.2011.02562.x, 2012.

Richardson, A. D., Hollinger, D. Y., Burba, G. G., Davis, K. J., Flanagan, L. B., Katul, G. G., William Munger, J., Ricciuto, D. M., Stoy, P. C., Suyker, A. E., Verma, S. B., and Wofsy, S. C. A multi-site analysis of random error in tower-based measurements of carbon and energy fluxes, Agric. For. Meteorol., 136, 1–18, 2006.

Ross, A., Smith, C. D., and Barr, A.: An improved post-processing technique for automatic precipitation gauge time series, Atmos. Meas. Tech., 13, 2979–2994, https://doi.org/10.5194/amt-13-2979-2020, 2020.

Sellers, P. J., Hall, F. G., Kelly, R. D., Black, T. A., Baldocchi, D., Berry, J., Ryan, M., Ranson, K. J., Crill, P. M., Lettenmaier, D. P., Margolis, H., Cihlar, J., Newcomer, J., Fitzjarrald, D., Jarvis, P. G., Gower, S. T., Halliwell, D., Williams, D., Goodison, B., Wickland, D. E., and Guertin, F. E.: BOREAS in 1997: Experiment overview, scientific results and future directions. J. Geophys. Res. 102, 28731-28770. https://doi.org/10.1029/97JD03300, 1997.

Smith, C. D., Ross, A., Kochendorfer, J., Earle, M. E., Wolff, M., Buisan, S., Roulet, Y.-A., and Laine, T.: Evaluation of the WMO Solid Precipitation Intercomparison Experiment (SPICE) transfer functions for adjusting the wind bias in solid precipitation measurements. Hydrology and Earth System Sciences, 24, 4025-4043, doi.org/10.5194/hess-24-4025-2020, 2020.

Smith, C. D., Yang, D., Ross, A., and Barr, A.: The Environment and Climate Change Canada solid precipitation intercomparison data from Bratt's Lake and Caribou Creek, Saskatchewan. Earth Syst. Sci. Data Special Issue, 11(3), 1337–1347, https://doi.org/10.5194/essd-11-1337-2019, 2018.

Sonnentag, O., van der Kamp, G., Barr, A. G., and Chen, J. M.: On the relationship between water table depth and water vapor and carbon dioxide fluxes in a minerotrophic fen, Global Change Biology, 16, 1762-1776, https://doi.org/10.1111/j.1365-2486.2009.02032.x, 2010.

Stephens J., Black, T. A., Jassal, R., Nesic, Z., Grant, N., Barr, A., Helgason, W., Richardson, A., Johnson, M., and Christen, A.: Effects of forest tent caterpillar defoliation on carbon and water fluxes in a boreal aspen stand, Agric. For Meteorol., 253-254, 176-189, https://doi.org/10.1016/j.agrformet.2018.01.035, 2018.

Suyker, A. E., Verma, S. B., and Arkebauer, T. J.: Season-long measurement of carbon dioxide exchange in a boreal fen, J. Geophys. Res., 102, 29021-29028, https://doi.org/10.1029/97JD03877, 1997.

Twine, T. E., Kustas, W. P., Norman, J. M., Cook, D. R., Houser, P., Meyers, T. P., Prueger, J. H., Starks, P. J., and Wesely, M. L.: Correcting eddy-covariance flux underestimates over a grassland, Agric. For. Meteorol., 103, 279-300, http://dx.doi.org/10.1016/S0168-1923(00)00123-4, 2000.

Water Survey of Canada: https://www.canada.ca/en/environment-climate-change/services/water-overview/quantity/monitoring/survey.html, 2023.

Wohlfahrt, G., Irschick, C., Thalinger, B., Hörtnagl, L., Obojes, N., Hammerle, A.: Insights from independent evapotranspiration estimates for closing the energy balance: a grassland case study. Vadose Zone J., 9, 1025-1033, https://doi.org/10.2136/vzj2009.0158, 2010.

https://doi.org/10.5194/essd-2024-492
Preprint. Discussion started: 26 June 2025

Yang, P. C., Black, T. A., Novak, M. D., Nesic, Z., Chen, Z., Neumann, H. H., and Blanken, P.D.: Spatial and temporal variability of CO_2 concentration and flux in a boreal forest. J. Geophys. Res., 104, 27,653-27,661, https://doi.org/10.1029/1999JD900295, 1999.

Zha T., Barr, A. G., Black, T. A., McCaughey, J. H., Bhatti, J., Hawthorne, I., Krishnan, P., Kidston, J., Saigusa, N., Shashkov, A., Nesic, Z.: 2009. Carbon sequestration in boreal jack pine stands following harvesting. Global Change Biology, 15, 1,475-1,487, https://doi.org/10.1111/j.1365-2486.2008.01817.x, 2009.